This is a repository copy of *Rigid-plastic membrane response of thin plates under impulsive blast loads using the extended Hamilton principle*.

White Rose Research Online URL for this paper:
https://eprints.whiterose.ac.uk/209255/

Version: Published Version

Rigid-plastic membrane response of thin plates under impulsive blast loads using the extended Hamilton principle

Saud A.E. Alotaibi [a,b,*,1], Samuel E. Rigby [a], Maurizio Guadagnini [a], Andrew Tyas [a]

[a] *Department of Civil & Structural Engineering, University of Sheffield, Mappin Street, Sheffield, S1 3JD, UK*
[b] *Department of Civil Engineering, Qassim University, Buraydah, Saudi Arabia*

ARTICLE INFO

ABSTRACT

The response of plates subjected to blast loads is of considerable scientific interest. The loading imparted to a structure following a close-in detonation of a high explosive is typically high in magnitude, near-impulsive, spatially non-uniform, with localised variability and a high dependence on factors such as charge shape, position, and composition. The resulting structural response may induce large displacements in materials whose properties may not be fully characterised. In order to properly account for the effects of such intrinsic and extrinsic uncertainties, modelling approaches must balance the competing demands of accuracy and low computational demand. This article applies the extended Hamilton's principle to rigid-plastic thin plates subjected to impulsive blast loads to derive the governing equation of motion without a prior assumption of the initial specific impulse distribution. Closed-form solutions to predict the plastic response are derived for rectangular and circular plates. The analytical models for uniform specific impulses are found to be in good agreement with high-fidelity numerical simulations performed using LS-DYNA and experimental data available in the literature.

1. Introduction

There is significant scientific interest in studying the structural response in the inelastic range when structures are subjected to extreme dynamic loadings, such as missile impacts and explosions. Extremely high magnitudes and short durations characterise these loads, see [1–4], and are expected to cause mainly plastic deformations in the structures.

Tyas and Rigby and their collaborators [1–3,5] provide experimental evidence that near-field blasts generate spatially non-uniform spontaneous pressures that, subsequently, decay exponentially. Such intense loading could induce large displacement, strain rate-dependent, and material failure effects in the structural response, see, e.g., Jones [6].

For these reasons, in addition to geometric complexities and boundary effects, the blast analyst typically resorts to making use of hydrocodes and Finite Element (FE) programs, attempting to simulate the complete problem. However, such an approach is computationally expensive. The challenge becomes more critical if we recognise that the input data of the blast threat are never known in advance, as pointed out by Tyas [3]. Furthermore, the material characteristics are prone, to some extent, to potential variabilities. Thus, to design robust structures,

it is more appropriate not to perform a single simulation but rather a large number of analyses, to fully characterise the likely response and associated confidence intervals. What, then, suits the analyst in this regard is the availability of models that can be evaluated more efficiently.

The present work aims to develop an analytical model to predict the response of thin ductile plates under impulsive blast loads. To this end, the current knowledge about the physical problem (see Section 2) is utilised while attempting to minimise the complexity of the problem.

First, the load is assumed to be perfectly impulsive and, thus, specified in terms of an initial velocity field derived from the prescribed blast-induced specific impulse. According to the UFC 3-340-02 design manual [7], the impulsive regime applies when the time to maximum response to load duration ratio is greater than three, see Figure 1–7 of the manual. Secondly, the material is idealised as rigid-perfectly plastic, which obeys von Mises's yield function and its associated flow rule. Finally, the plate, which is restrained along its outer periphery, is assumed to deform in membrane mode without in-plane displacements; hence, flexural effects are ignored.

The first assumption, due to Rigby et al. [8], is fundamental to the present analysis (the absence of externally applied forces ensures a monotonic deformation path in a rigid-plastic structure, as will be discussed in Section 3). The last assumption is based on the membrane thinness and loading intensity.

---

* Corresponding author at: Department of Civil & Structural Engineering, University of Sheffield, Mappin Street, Sheffield, S1 3JD, UK.
E-mail address: salotaibi2@sheffield.ac.uk (S.A.E. Alotaibi).
[1] PhD candidate.

The well-known extended Hamilton's principle, see, e.g., [9,10], is applied to the above described problem to obtain the appropriate equation of motion governing the transverse displacement of the thin membrane. The equation is found as a two-dimensional linear wave equation. Therefore, it is solved by the modal decomposition technique while enforcing Drucker's [11,12] postulate of the plastic work nonnegativity. Analytical solutions are provided for rectangular membranes subjected to arbitrary distribution of specific impulse and for axisymmetric circular membranes.

The closed-form solutions for rectangular and circular membranes loaded by uniform impulses are compared to experimental data found in Nurick, Martin and Pearce [13], Gharababaei and Darvizeh [14], and Nurick, Gelman, and Marshall [15]. In addition, the analytical solution is compared to results from LS-DYNA [16] simulations, where the loads are prescribed through the initial velocity field according to Rigby et al. [8] and using relevant material parameters adopted from [8,17,18]. Finally, the present model is compared to an existing model proposed by Yuen et al. [19] as a modification to Nurick and Martin's [20] model. The uniform and non-uniform impulse solutions are found to be reasonably accurate with very low computational expense.

2. Literature review

2.1. Background

The field of investigating the response of engineering structures under intense dynamic loads has attracted the interest of many researchers. By far, the idealisation of a rigid-plastic material behaviour has been the basic framework based on which several approximate closed-form solutions were obtained. In earlier works, responses to uniform dynamic pressure and uniform impulse were the main topic. Both small and large displacement regimes were considered in the response of circular and rectangular plates and beams with various boundary conditions.

Again, structures were idealised as rigid-plastic, and the particular spatial form of the dynamic load is assumed a priori. The first step is to find the "quasi-static" limit load by means of the upper and lower limit analysis theorems and to assume the incipient collapse mechanism. The mechanism should be consistent with the underlying yield function, its associated flow rule, and boundary conditions. At the static collapse load, motion follows the "quasi-static" mechanism. As the dynamic load intensity increases further, determination of the resulting dynamic mechanism becomes highly involved, and hence it is typically assumed. Then, the exact dynamic equilibrium equation is formulated in which the acceleration derives from the assumed collapse mechanism. The equation is then solved while avoiding any violation of the yield condition and the flow rule. If yield violation cannot be avoided, then the initially assumed mechanism is wrong. In this case, another initial mechanism must be chosen, and the process is repeated. The solution is valid when equilibrium, yield conditions, flow rule, and boundary conditions are all satisfied. Thin plates are found to initially respond in flexure, and as displacement increases further, membrane effects evolve and become dominant. The load-free membrane response is typically driven by some initial displacement and velocity conditions, which are the final states of the initial flexural phase of response.

Typically, the eventual correct solution could be associated with a "dynamic" collapse mechanism that is substantially different from the "quasi-static" mechanism. Since the material is rigid-plastic, then motion will eventually end, which happens when the external loads are removed and the instantaneous velocity is zero everywhere (i.e. current kinetic energy and external work are simultaneously zero).

The methodology behind the earlier works has been continued recently where non-uniform blast loads are also studied. However, the so-obtained solutions apply to the initially specified spatial forms of the loading function. Response to arbitrary loading has not been obtained. Furthermore, no solution for membranes' responses due to initial conditions imposed directly by the blast load is available.

2.2. Analytical models

A subset of earlier and recent publications that studied the dynamic response of rigid-plastic structures under extreme dynamic loadings (e.g. blast and impact) is summarised in Table 1. For more discussion of the analytical method and for additional references, the reader is referred to [21–25], and [26].

Martin and Symonds [41] developed the mode approximation technique to predict the response of rigid-plastic structures. Martin [40] showed that the motion of an impulsively loaded structure eventually converges to a mode-form response. The current practice of simplified blast analysis, which is adopted in [7] and applied in Rigby et al. [52], is also a mode approximation technique. This single-degree-of-freedom SDOF technique is originally developed by Biggs [53].

In an analytical and experimental work, Nurick and Martin [20, 54] derived a non-dimensional impulse (or a damage number) that correlates linearly with the normalised permanent displacements of rectangular and circular thin plates obtained from a large set of experimental data. Their model was revised (25 years later) by Nurick and his colleagues [19]. The model applies to plates loaded by impulses of constant amplitudes.

Cloete and Nurick [46] hypothesised that a quadratic displacement field can be assumed to analyse a uniformly loaded thin plate. Using such field, the authors solved the problem of a circular membrane loaded with uniform impulse. They found that the central residual transverse displacement varies linearly with Nurick and Martin's non-dimensional impulse. Moreover, it was shown that such displacement is independent of the "in-plane" components of displacement.

In studying the response of thin plates under non-uniform blast loads, Tyas, Rigby, and co-authors [8,55] established two important relationships. Firstly, the local initial velocity, $\dot{w}_0$, of the target (with density ρ, thickness h, and exposed area A) is confirmed to be a linear function of the imparted non-uniform specific impulse field, i,

$$\dot{w}_0 = \frac{i}{\rho h},$$

which is based on the upper bound kinetic energy. That is, non-uniform specific impulse generates non-uniform initial velocity, see Fig. 1(c). This initial velocity field contrasts with the "lower-bound" initial velocity field,

$$\dot{w}_{0,lb} = \frac{\int_A i\, dA}{\rho h A}.$$

which is uniform and is interpreted as the rigid-body velocity (i.e. total impulse divided by total mass), see Fig. 1(b).

Secondly, the maximum permanent displacement is a linear function of the energy-equivalent uniform total impulse, I_k, which is also based on the upper bound kinetic energy uptake, K_{ub}, developed by Tyas and Pope [5], see Fig. 1,

$$K_{ub} = \frac{1}{2\rho h} \int_A i^2\, dA, \quad \text{and} \quad I_k = \sqrt{A \int_A i^2\, dA}.$$

The authors showed that the blast load can be replaced by a prescribed initial velocity field, which remarkably simplifies the analysis. This observation highlights the importance of the actual spatial variation of the specific impulse. According to the authors, the imparted energy from the blast onto a thin plate cannot be higher than K_{ub} or lower than the kinetic energy computed with $\dot{w}_{0,lb}$, provided the regime is impulsive.

Pannell et al. [56] proposed a model that predicts the non-uniform distribution of specific impulses arising from near-field blasts with scaled distances of 0.11–0.55 m/kg$^{1/3}$. Determining the specific impulse profile is critical in analysing structures under near-field blast loading, as discussed in [8].

Table 1
Analytical works to study the dynamic response of rigid-plastic structures under extreme dynamic loadings.

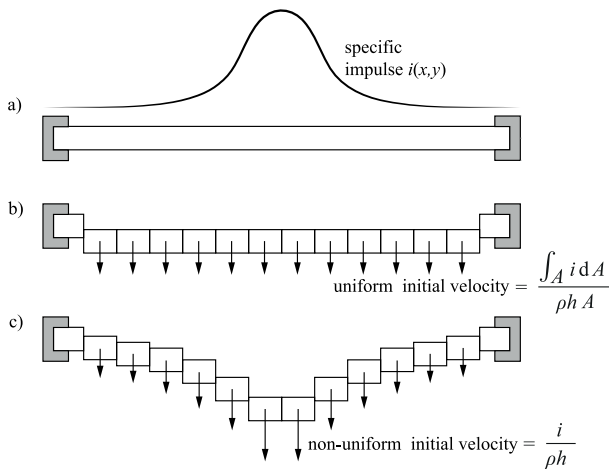|	Circular plate	Rectangular plate	Beam	Theory
Small displacement (flexure)	[27–31]	[32,33]	[34–37]	[38–41]
Large displacement (membrane)	[5,8,42–46]	[14,26,47–49]		[50,51]

Fig. 1. Non-uniform specific impulse distribution (a) and the generated profile of initial velocity assuming a lower-bound (b) and an upper-bound (c) kinetic energy uptake, reproduced after Tyas and Pope [5].

2.3. Experimental results

Nurick and his collaborators [13,15,54,57,58] presented extensive experimental data for circular and rectangular plates under uniform impulsive loads.

As discussed in Section 1, the team of the Blast and Impact Engineering research group at the University of Sheffield [1–3,5] confirmed experimentally that near-field blasts produce spatially non-uniform specific impulses. Furthermore, the researchers and their collaborators presented experimental and numerical studies of the transient deformation of thin ductile plates subjected to near-field blast [55]. In their study, both the blast load and the full-field transient displacement of the target were measured locally: (a) the dynamic pressures histories at different spatial points were measured by the Characterisation of Blast Loading (CoBL) apparatus [2,59], providing the spatial variations of the specific impulses; (b) full-field transient displacements of the targets were measured using high-speed imaging, described further in [18]; and (c) the total impulse was measured using a ballistic pendulum.

Also, Langdon and her collaborators [18,60,61] studied the response of steel plates under near-field blast experimentally. It was observed that a localised blast load induces central dishing (or bulging) in the targets. Gharababaei and Darvizeh [14] performed blast experiments on steel, aluminium, and copper thin circular plates which were loaded by detonating thin cylindrical charges of high explosives. The authors used rigid tubes to guide the propagation of the shock waves as they travel towards the specimens. Large plastic deformations were observed in the tests.

In addition, Aune and his team presented experimental and numerical studies on the response of thin plates under free-air blasts [62,63] and blasts produced in a shock tube facility [64]. Additional air-blast experiments are also reported by Spranghers et al. [65,66]. The plates are made of ductile materials (structural steel and aluminium) and were observed to respond impulsively and plastically.

2.4. Aims of the present study

The above discussion serves as a short account of some notable works investigating the response of simple structures to blast loads. As mentioned, some discuss the theory and provide analytical solutions, while others give experimental observations to strengthen or refine the theory.

Commercially available FE programs can simulate the nonlinear structural response under specific blast settings [8,17,63,66,67]. However, such approach is computationally expensive and requires significant user expertise. Furthermore, extra computations might be necessary to ensure the solution is insensitive to any artificial parameters that are not pertinent to the physical problem (e.g. those related to hourglassing, artificial damping, structural and material locking, extra contact and leakage controls, etc.) Therefore, the approach is not directly suitable for probabilistic-based blast analyses that require many repeated calculations. The situation takes us back to the interest in building analytical solutions to idealised mechanical problems as they are more computationally efficient and fast-running. This is the rationale of the present work.

As discussed in Section 1, the present work aims to develop an analytical solution to predict the transient and permanent displacement of thin ductile plates subjected to impulsive blast loads. The model utilises the following simplifying idealisations: impulsive blast load, rigid-perfectly plastic material behaviour, and membrane mode of deformation, according to observations from the already discussed literature. We apply the extended Hamilton's principle to obtain a general equation of motion that applies to any target's geometry without a prior assumption on the initial field. The then-derived equation and solution will accommodate any distribution of the blast-induced specific impulse.

3. Theory

3.1. Problem definition

Consider a thin membrane made of a rigid-perfectly plastic metal that is subjected to a prescribed initial velocity field obtained from a specific impulse distribution according to Tyas and Pope [5] and Rigby et al. [8].

The membrane can be of a rectangular or circular geometry, and it is supported along its outer periphery. For the rectangular geometry, L_x and L_y are the sides' lengths, as indicated in Fig. 2, and R is the radius of the circular membrane. The specific impulse is denoted by $i(x, y)$ or $i(r)$, where x and y are the rectangular undeformed coordinates for rectangular geometry, whereas r is the radial undeformed coordinate for the circular membrane. Let t denotes time, and ρ, h, and σ_0 denote, respectively, density, thickness, and characteristic yield strength of the membrane.

The membrane is assumed to respond in pure membrane mode. Further, it is assumed that the components of displacement along the undeformed in-plane coordinates are negligible. That is, the only non-zero displacement is the one along the original out-of-plane coordinate, which is denoted by w. In other words, every particle of the membrane displaces vertically.

In line with the perfect plasticity assumption, the characteristic yield strength σ_0 is assumed constant. Thus, for materials exhibiting substantial work-hardening [64,68], σ_0 could be defined such that a rectangular stress-plastic strain curve preserves the total area under the actual uniaxial stress-plastic strain curve. This approach is adopted in the UFC 3-340-02 [7] manual.
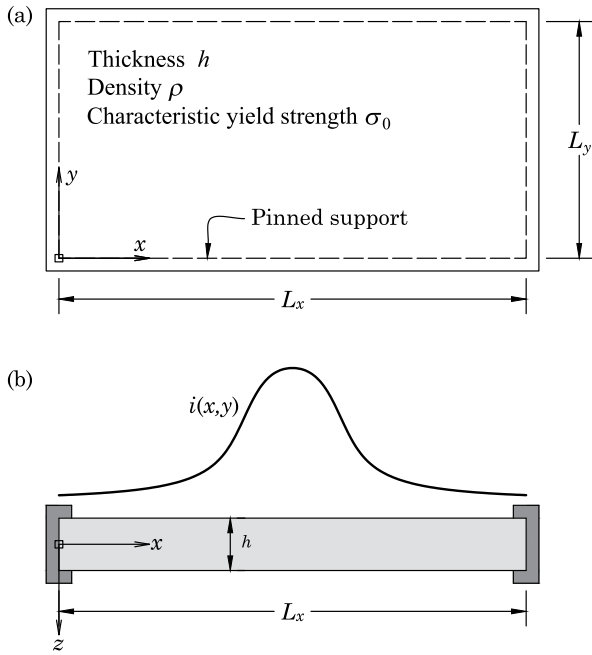
In the figure: specific impulse $i(x,y)$; uniform initial velocity $= \dfrac{\int_A i\,\mathrm{d}A}{\rho h A}$; non-uniform initial velocity $= \dfrac{i}{\rho h}$

(a)

(b)

Fig. 2. Problem definitions for the rectangular membrane: (a) plan view showing undeformed geometry and (b) side view showing a typical spatial distribution of specific impulse i.

3.2. Development of the equation of motion

The extended Hamilton's principle is applied to the present problem to systematically derive the equation of motion. In applying the principle, treatment of kinetic energy and external work (if any) terms are not new and will not be shown for brevity. However, the internal energy term needs special consideration. First, there is no elastic strain energy in the system, and the only allowed internal energy (arising from the accumulation of plastic deformation) is dissipative in nature. To obey such irreversible behaviour, the rate of plastic work must always be non-negative [11,12]. That is, when strain rate tends to change sign, stress must instantly do so in a rigid-perfectly plastic structure.

In Hamilton's principle, the *total* internal energy is the one that should be included, not the *rate* of energy. The total energy is the time integral of the energy rate. However, the time integration can be carried out beforehand (i.e. explicitly) when the total plastic strain is monotonic since the stress would be constant in terms of sign (recall that its magnitude is already constant from the perfect plasticity). Now, since there are no external forces, the total plastic strain is guaranteed to be monotonic (i.e. the sign of strain rate is fixed) when the transverse velocity is monotonic.

In the following, σ_{ij}, s_{ij}, ε_{ij}, and λ are the stress, deviatoric stress, (Green–Lagrange) strain, and the plastic multiplier, respectively. A dot ($\cdot$) over a symbol denotes time differentiation, a repeated subscript implies summation, and a superscript (p) denotes the plastic part.

With reference to the von Mises's yield function, $f(\sigma_{ij}) = \frac{1}{2}s_{ij}s_{ij}$, yielding of the material occurs when $f(\sigma_{ij}) = \frac{1}{3}\sigma_0^2$. Associated with such yielding condition, the incremental flow rule reads

$$\dot{\varepsilon}_{ij}^p = \dot{\lambda}\frac{\partial f}{\partial \sigma_{ij}} = \dot{\lambda}s_{ij} \qquad \dot{\varepsilon}_{ij}^p \equiv 0 \text{ if } f(\sigma_{ij}) < \frac{1}{3}\sigma_0^2 \tag{3.1}$$

Now, if the material has actually yielded, i.e. $\dot{s}_{ij} \equiv 0$, then under a monotonic deformation regime, the flow rule can be integrated by parts (while taking advantage of $\dot{s}_{ij} = 0$ and assuming $\lambda|_{t=0} = 0$) to obtain

$$\varepsilon_{ij}^p = \int \dot{\varepsilon}_{ij}^p \, dt = \int \dot{\lambda}s_{ij} \, dt = \lambda s_{ij} - \int \lambda \dot{s}_{ij} \, dt = \lambda s_{ij}. \tag{3.2}$$

Eq. (3.2) allowed a transition from the flow to the total theory of plasticity, and it holds only when the path is monotonic. In fact, Drucker [12] assures that when loading is monotonic, the two plasticity theories are identical.

Using Eq. (3.2), it can be shown that $\lambda = \left(\sqrt{3/2\ \varepsilon_{ij}^p \varepsilon_{ij}^p}\right)/\sigma_0$, and the total plastic work, which is

$$W_p = \int_V \sigma_{ij}\varepsilon_{ij}^p \, dV, \tag{3.3}$$

can be expanded as $W_p = \int_V s_{ij}\varepsilon_{ij}^p \, dV = \int_V \lambda s_{ij}s_{ij} \, dV = \int_V \lambda \left(\frac{2}{3}\sigma_0^2\right) dV$, or

$$W_p = \int_V \sigma_0\sqrt{2/3\ \varepsilon_{ij}^p \varepsilon_{ij}^p} \, dV. \tag{3.4}$$

where the plastic incompressibility, $\varepsilon_{ii}^p = \lambda s_{ii} = 0$, of the von-Mises material was utilised.

From now on, the superscript p will be omitted as total strain and plastic strain are identical in line with the rigid-plastic assumption. To evaluate the quantity $\varepsilon_{ij}\varepsilon_{ij}$, the four non-vanishing strain components as functions of the transverse displacement, $w(x, y, t)$, will be utilised. These are

$$\varepsilon_x = \frac{1}{2}\left(\frac{\partial w}{\partial x}\right)^2, \quad \varepsilon_y = \frac{1}{2}\left(\frac{\partial w}{\partial y}\right)^2,$$

$$\gamma_{xy} = \frac{\partial w}{\partial x}\frac{\partial w}{\partial y} = 2\sqrt{\varepsilon_x\varepsilon_y}, \tag{3.5}$$

and from the incompressibility condition, one has

$$\varepsilon_z = -(\varepsilon_x + \varepsilon_y). \tag{3.6}$$

Then, through some algebra simplifications, it can be shown that

$$\varepsilon_{ij}\varepsilon_{ij} = 2(\varepsilon_x + \varepsilon_y)^2. \tag{3.7}$$

Therefore, the total plastic work under a monotonic deformation path becomes

$$W_p = \int_V \frac{2}{\sqrt{3}}\sigma_0(\varepsilon_x + \varepsilon_y) \, dV$$

$$= \int_V \frac{2}{\sqrt{3}}\sigma_0 \left[\frac{1}{2}\left(\frac{\partial w}{\partial x}\right)^2 + \frac{1}{2}\left(\frac{\partial w}{\partial y}\right)^2\right] dV. \tag{3.8}$$

It should be noted that the stress σ_{ij}, appearing in Eq. (3.3), is the second Piola–Kirchhoff stress since it is the work-conjugate to Green–Lagrange strain. However, for consistency of the formulation, the small strain assumption implies that this mentioned stress can be replaced with the true Cauchy stress. Hence, we refer to σ_{ij} throughout as the Cauchy stress.

Then, the extended Hamilton's principle is applied, which reads

$$\delta\left(\int_{t_1}^{t_2} H \, dt\right) = 0, \tag{3.9}$$

where δ is the variational operator, and t_1 and t_2 are arbitrary times. In Eq. (3.9), the Hamiltonian, H, of the system (in absence of external work and elastic strain energy) is given by

$$H = [K - W_p]. \tag{3.10}$$

in which K is the total kinetic energy of the membrane, which is $K = \int_V \frac{1}{2}\rho\dot{w}^2 \, dV$, and W_p was given in Eq. (3.8). Notice that H becomes a functional of w only.

Finally, by (i) applying δ on w, (ii) carrying out spatial and temporal integration by parts, (iii) imposing constraints on w at the membrane edges and anywhere at times t_1 and t_2 where δw vanishes identically, and (iv) requiring δw to be otherwise arbitrary, then one obtains the (Euler–Lagrange) equation of motion governing the response of the rigid-perfectly plastic membrane as

$$\frac{2}{\sqrt{3}}\sigma_0\left[\frac{\partial^2 w}{\partial x^2} + \frac{\partial^2 w}{\partial y^2}\right] = \rho\ddot{w}. \tag{3.11}$$

Eq. (3.11) is a two-dimensional scalar (plastic) wave equation in $w(x, y, t)$ in a rectangular coordinate system and with a wave speed $\left[2\sigma_0/(\sqrt{3}\rho)\right]^{1/2}$. Note that Eq. (3.11) is a field equation so that it applies to any membrane geometry with restrained edges.

Later, the equation is solved for a rectangular membrane, as defined in Fig. 2, under the following kinematic conditions

$$w(0, y, t) = w(L_x, y, t) = w(x, 0, t) = w(x, L_y, t) = 0,$$

$$w(x, y, 0) = 0, \tag{3.12}$$

and the dynamic condition

$$\dot{w}(x, y, 0) = \frac{i(x, y)}{\rho h}. \tag{3.13}$$

Eq. (3.13) is experimentally shown to hold for thin plates under non-uniform specific impulse [5,8,55], which was derived from the balance of linear momentum of shear non-rigid thin plates.

For a circular membrane and under axisymmetric conditions (which will be assumed throughout), it can be shown, through the standard transformation from rectangular to polar coordinates, that the equation of motion is given as

$$\frac{2}{\sqrt{3}}\sigma_0 \left[\frac{\partial^2 w}{\partial r^2} + \frac{1}{r}\frac{\partial w}{\partial r}\right] = \rho \ddot{w}. \tag{3.14}$$

where a term within the brackets on the left-hand side $(1/r^2)\,\partial^2 w/\partial\theta^2$ has been omitted due to the axisymmetric assumption. Eq. (3.14) will be solved under the following conditions

$$w(R, t) = w(r, 0) = 0, \quad \dot{w}(r, 0) = \frac{i(r)}{\rho h}. \tag{3.15}$$

Although the actual problem involves plastic deformations, the obtained equations of motion are linear. Hence, they can be solved by Fourier's decomposition, which is based on the principle of superposition.

It should be recalled that the above equations of motion are valid as long as the deformation path remains monotonic so that Eq. (3.2) is not violated. Hence, the solutions (to be presented later) of Eqs. (3.11) and (3.14) are valid up to the instant of time when the transverse velocity, $\dot{w}$, tends to change sign, or simply when velocity reaches zero. In other words, a component of the solution must terminate whenever the velocity associated with it reaches zero for the first time. Otherwise, plastic work would decrease and thereby violating its irreversibility or dissipating nature, and thus the solution becomes non-physical.

Many textbooks, e.g. references that treat the elastic free vibration of pre-tensioned membranes under small displacements, such as [69, Ch. IX] or [70, Sec. 69], show how equations similar to Eqs. (3.11) and (3.14) can be solved. Excellent stepwise derivations are presented in [71]. Hence, the derivation steps of the solution will be omitted for brevity. Instead, the solutions themselves are given.

4. Rectangular membrane

4.1. Response of rectangular membrane

The rectangular membrane equation of motion, Eq. (3.11), was solved by the modal decomposition technique under the prescribed geometric conditions, Eqs. (3.12) and (3.13). Its solution is

$$w(x, y, t) = \frac{4}{\rho h L_x L_y} \sum_{m,n=1}^{\infty} \frac{I_{mn}}{\omega_{mn}} \phi_{mn}(x, y) \sin\left(\omega_{mn} t\right) \tag{4.1}$$

with the wave speed c, mode shape $\phi_{mn}(x, y)$, modal angular frequency ω_{mn}, and total modal impulse I_{mn} given by

$$c = \sqrt{\frac{2}{\sqrt{3}}\frac{\sigma_0}{\rho}} \tag{4.2}$$

$$\phi_{mn}(x, y) = \sin\left(\frac{m\pi x}{L_x}\right) \sin\left(\frac{n\pi y}{L_y}\right)$$

$$\omega_{mn} = \frac{\pi c}{L_x L_y}\sqrt{(L_y m)^2 + (L_x n)^2} \tag{4.3}$$

$$I_{mn} = \int_0^{L_x}\int_0^{L_y} i(x, y)\sin\left(\frac{m\pi x}{L_x}\right)\sin\left(\frac{n\pi y}{L_y}\right) dy\,dx. \tag{4.4}$$

The pair (m, n) defines a particular mode with mode shape $\phi_{mn}(x, y)$. It is known that the modes are orthogonal over the membrane domain, and hence they are independent. Thus, to fulfill the requirement of a monotonic deformation path (and hence obey the plastic work's non-negativity), a strategy is adopted to enforce the termination of a particular mode when the associated (modal) velocity reaches zero for the first time. This occurs when

$$t = t_{m,n} = \frac{\pi}{2\omega_{mn}}. \tag{4.5}$$

From ω_{mn}, see Eq. (4.3), it is clear that the sequence of turning off the modal contributions is ordered from highest to lowest modes in terms of frequency. The notion of sequential terminations of the modes was previously used in [43,45]. The last contributing mode is the first, i.e. with $(m = n = 1)$. Thus, the whole membrane ceases motion at no later than $t = t_{1,1}$, which is given by

$$t_{1,1} = \frac{L^*}{2c} \tag{4.6}$$

where L^*, defined for convenience, is the ratio of the membrane area to the length of its diagonal and given by

$$L^* \equiv \frac{L_x L_y}{\sqrt{L_x^2 + L_y^2}}. \tag{4.7}$$

Note that if $t_{1,1}$ is less than three times the duration of blast load, the global response is less likely to be impulsive, based on [7], since $t_{1,1}$ is an upper bound on the response time. The actual time of maximum response is the modal time $t_{m,n}$ of the dominant mode (whose total modal impulse is I_{mn}) of the membrane under a particular distribution of specific impulse i. If there are several dominant modes, then the maximum time is the largest $t_{m,n}$ among these modes.

The permanent shape, $w_p(x, y)$, of the membrane is given by $w(x, y, t)$ when $t \geq t_{1,1}$, or

$$w_p(x, y) = \frac{4}{\pi\rho c h} \sum_{m,n=1}^{\infty} \frac{I_{mn}}{\sqrt{(L_x n)^2 + (L_y m)^2}} \phi_{mn}(x, y). \tag{4.8}$$

For all cases in which the specific impulse distribution is symmetric about the membrane's centre, the peak displacement is located at the centre. The central permanent displacement, $w_c \equiv w_p(L_x/2, L_y/2)$, is

$$w_c = \frac{4}{\pi\rho c h} \sum_{m,n=1}^{\infty} \frac{I_{mn}}{\sqrt{(L_x n)^2 + (L_y m)^2}} \sin\left(\frac{m\pi}{2}\right)\sin\left(\frac{n\pi}{2}\right). \tag{4.9}$$

According to Pannell et al. [56], the specific impulse distribution from a near-field spherical charge blast is of a Gaussian form as a function of the angle of incidence. However, it was not possible to evaluate I_{mn} symbolically for a specific impulse distribution, $i(x, y)$, as predicted by Pannell et al. Hence, numerical integration is needed. A practical MATLAB code for calculating I_{mn} using the Fast Fourier Transform (FFT) is given in Appendix B.

Fig. 3 shows the normalised permanent displacement, w_p, profiles along $y = L_y/2$ due to three impulse distributions with constant amplitudes applied over varying central areas of a rectangular membrane. In the figure, the legends indicate the ratios of the loaded to total areas. It is, thus, evident that a localised impulse induces localised displacement shape, i.e. with central dishing, while the case of uniform impulse applied over the whole area of the membrane results in global uniform dishing.

In practice, a finite number of modes is used to numerically evaluate the permanent, $w_p(x, y)$, and permanent central, w_c, displacements. To maintain sufficient accuracy while truncating the infinite series in Eqs. (4.8) and (4.9), the error estimate given in Appendix A can be
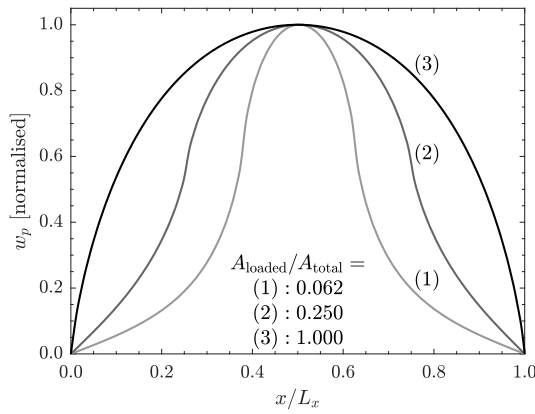
Fig. 3. Permanent displacement profile for rectangular membrane under three sets of impulses of constant amplitudes applied over central rectangular regions with loaded-to-total area ratios of (1) 0.062, (2) 0.25, and (3) 1.0. Curve (1) is associated with localised impulse, and (3) results from a uniform impulse over the entire membrane.
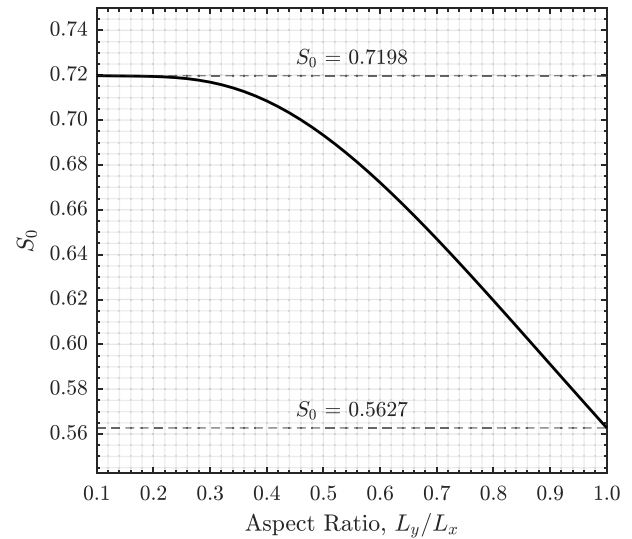

Fig. 4. The converged value of truncated sum, S_0, for the rectangular membrane associated with uniform impulse case as a function of the membrane aspect ratio, L_y/L_x, where $L_y \leq L_x$.

used. The error relates the sum of modal impulses (included in the approximation) to the energy-equivalent total impulse, I_k which is

$$I_k = \sqrt{A \int_A i^2 \, dA}$$

in which A is the area of the membrane. The absolute importance of a particular mode is shown to be indicated by the measure $0 \leq (2I_{mn}/I_k)^2 \leq 1$, which can also be used to identify the dominant mode(s); dominant modes have values closer to unity.

4.2. Uniform specific impulse case — rectangular membrane

For the case where the specific impulse has a constant distribution, i.e. $i(x, y) = i_0$, the modal impulse, I_{mn}, simplifies to

$$I_{mn} = \begin{cases} \dfrac{4i_0 L_x L_y}{\pi^2 \, mn} & \text{when } (m, n) \text{ are odd} \\ 0 & \text{otherwise} \end{cases}$$

which suggests that the first mode is the most dominant.

The peak displacement is located at the plate's centre and is given by

$$w_c = \frac{16i_0 L_y}{\pi^3 \rho c h} \sum_{m,n=1,3,5}^{\infty} \frac{\sin\left(\frac{m\pi}{2}\right) \sin\left(\frac{n\pi}{2}\right)}{mn\sqrt{n^2 + m^2 (L_y/L_x)^2}}. \tag{4.10}$$

In Eq. (4.10), the summand depends only on the membrane's aspect ratio L_y/L_x. Denoting the sum by S_0, it was observed to converge. The value of S_0 for any aspect ratio in the range $[0.1 - 1.0]$ can be read from Fig. 4, in which $L_y \leq L_x$.

With S_0 known, the central displacement of a membrane due to a uniform impulse (with intensity i_0) is given by

$$w_c = \frac{16i_0 L_y}{\pi^3 \rho c h} S_0. \tag{4.11}$$

Or, using the total impulse $I_0 = \int_A i(x, y) \, dA = A i_0$, the last expression becomes

$$w_c = \frac{16 S_0}{\pi^3 \rho c h L_x} I_0 \equiv k_0 I_0 \tag{4.12}$$

where a structural parameter k_0 was introduced and defined as

$$k_0 = \frac{16 S_0}{\pi^3 \rho c h L_x}. \tag{4.13}$$

It should be re-emphasised that L_y is the shorter side's length, i.e. $L_y/L_x \leq 1$, when S_0 is estimated from Fig. 4.

5. Circular membrane

5.1. Response of circular membrane

As stated in Section 3, axisymmetric conditions are assumed for the circular membrane problem. Eq. (3.14) was solved by the modal decomposition technique. The solution is presented below, Eq. (5.1), which gives the displacement of a circular rigid-perfectly plastic membrane of radius R, mass density ρ, characteristic yield strength σ_0, and thickness h, due to a specific impulse (impulse per unit area), $i(r)$.

$$w(r, t) = \frac{2}{\rho c R h} \sum_{m=1}^{\infty} \frac{I_m}{j_{0,m} J_1(j_{0,m})^2} \phi_m(r) \sin(\omega_m t), \tag{5.1}$$

where

$$\phi_m(r) = J_0\left(\frac{j_{0,m}}{R} r\right), \tag{5.2}$$

$$\omega_m = \frac{c j_{0,m}}{R}, \tag{5.3}$$

$$I_m = \int_0^R i(r) J_0\left(\frac{j_{0,m}}{R} r\right) r \, dr \tag{5.4}$$

I_m is the total modal impulse per unit radian, c is the wave speed given in Eq. (4.3), $\phi_m(r)$ is the mth mode shape, and ω_m is the corresponding frequency. In above, $J_0(x)$ and $J_1(x)$, respectively, are Bessel *functions* of the first kind of order zero and one, while the *scalar* value $j_{0,m}$ is the mth root of $J_0(x) = 0$, i.e. $J_0(j_{0,m}) \equiv 0$. The solution does not involve Bessel functions of the second kind to avoid infinite (non-physical) response at the origin (plate's centre). Furthermore, the modal solution depends only on the zeroth order Bessel function due to the axisymmetry of the problem. Again, the mth mode shape is $J_0(j_{0,m} r/R)$, and the square of its norm (per unit radian) is $(1/2)R^2 \left[J_1(j_{0,m})\right]^2$. The modes, $\phi_m(r)$, are orthogonal to each other, and thus they are independent.

Similar to the rectangular case, the contribution from a given mode in the solution is valid until the corresponding modal velocity reaches zero when $t \geq t_m$, where $t_m = \pi R/(2c j_{0,m})$. Thus, the modes will be switched off sequentially in descending order with respect to frequency. Thus, the whole membrane motion terminates at or before $t = t_1 = \pi R/(2c j_{0,1})$, where $j_{0,1} = 2.405$.

Table 2
The first seven roots of the zeroth-order Bessel function $J_0(x)$ and their related quantities, computed using [72].

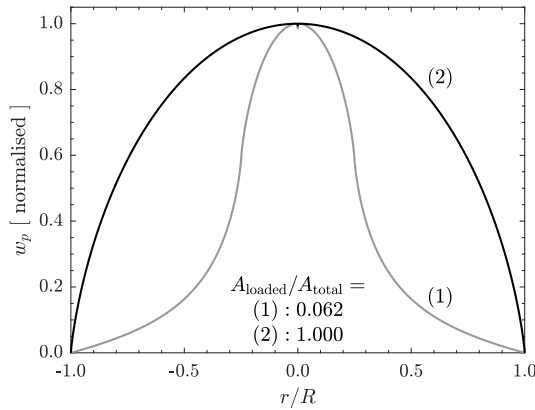| m	1	2	3	4	5	6	7
$j_{0,m}$	2.4048	5.5201	8.6537	11.7915	14.9309	18.0711	21.2116
$J_1(j_{0,m})^2$	0.2695	0.1158	0.0737	0.0540	0.0427	0.0352	0.0300
$J_1(j_{0,m})/j_{0,m}$	0.2159	−0.0616	0.0314	−0.0197	0.0138	−0.0104	0.0082

Fig. 5. Permanent displacement profile of an axisymmetric circular membrane subjected to a uniform impulse which is applied over a localised region (1) with a loaded-to-total area ratio of 0.062 and over the whole area (2) of the membrane as predicted by the present solution.

The permanent membrane profile, $w_p(r)$, is obtained from Eq. (5.1) for $t \geq t_1$ and is given by

$$w_p(r) = \frac{2}{\rho c R h} \sum_{m=1}^{\infty} \frac{I_m}{j_{0,m} J_1(j_{0,m})^2} \phi_m(r). \tag{5.5}$$

Since the problem is axisymmetric, the central displacement is the peak. Using the fact that $J_0(0) = 1$, the central permanent displacement, $w_c \equiv w_p(r = 0)$, is

$$w_c = \frac{2}{\rho c R h} \sum_{m=1}^{\infty} \frac{I_m}{j_{0,m} J_1(j_{0,m})^2}. \tag{5.6}$$

Some available tools, e.g. MATLAB native function besselj() and the user-built MATLAB function in [72], can be utilised to evaluate Bessel quantities appearing in the above expressions. Table 2 is provided for quick estimation purposes.

Similar to the rectangular case, it was not possible to evaluate the integral I_m for a specific impulse distribution, $i(r)$, of the type predicted by Pannell et al.'s [56] model. Thus, I_m needs to be computed numerically.

Experiments indicate that when a circular membrane is subjected to localised impulse, say, over the membrane's central region, then central dishing results, see Curry and Langdon [18]. Thus, to qualitatively test the developed solution, such a loading case was simulated that results in the permanent shape depicted in Fig. 5 by curve (1), in which a central bulging can be seen.

5.2. Uniform specific impulse case — circular membrane

When the specific impulse (impulse per unit area) is spatially uniform with intensity i_0, the total modal impulse I_m simplifies to $I_m = [i_0 R^2 J_1(j_{0,m})]/j_{0,m}$.

In this case, the permanent central displacement of a circular membrane is

$$w_c = \frac{2Ri_0}{\rho c h} \sum_{m=1}^{\infty} \left[j_{0,m}^2 J_1(j_{0,m}) \right]^{-1}$$

$$= \frac{2Ri_0}{\rho c h} S_0 \tag{5.7}$$

in which the numerical value of the infinite sum is denoted with S_0 and evaluates to 0.2674. Hence, the central permanent displacement of a circular membrane due to a uniform specific impulse (of intensity i_0) is

$$w_c = \frac{2Ri_0}{\rho c h} \times 0.2674. \tag{5.8}$$

Alternatively, in terms of total impulse $I_0 = \pi R^2 i_0$, the central displacement becomes

$$w_c = \frac{2 \times 0.2674}{\pi R \rho c h} I_0 \equiv k_0 \times I_0 \tag{5.9}$$

with the circular structural parameter k_0 defined as

$$k_0 = \frac{2 \times 0.2674}{\pi R \rho c h}. \tag{5.10}$$

The model predicts the normalised permanent membrane profile for the uniform specific impulse case as shown by curve (2) in Fig. 5, presented earlier.

6. Model verification

6.1. Rectangular model verification

6.1.1. Uniform impulse

The solution w_c for the uniform impulse case, as given by Eq. (4.12), is validated using experimental data obtained from the literature as detailed in this section. Nurick, Martin, and Pearce [13] carried out 82 experiments using rectangular and square thin plates made of steel, and the specimens were loaded impulsively by distributed sheets of explosives. The authors suggest that the impulse distributions are uniform over the specimens' exposed surfaces. The sides measured 113 mm and 70 mm for the rectangular plates, and a side length of 89 mm was given for the square plates. The thickness and static yield strength were given as 1.6 mm and 296 MPa, respectively; the mass density is assumed to be 7830 kg/m³. In the tests, the amounts of explosives were varied, resulting in different values of total impulses measured using a ballistic pendulum. The permanent central displacements were measured and given in the paper, and further details can be found there.

Nurick et al. [13] data is used to validate the solution, Eq. (4.12). The static yield strength reported in the experiments is taken as σ_0 in the model. The results of the comparisons are shown in Figs. 6 and 7.

Nurick et al. experiments were simulated numerically using LS-DYNA [16], in which the plates were subjected to uniform initial velocity fields. The steel material was modelled using the *MAT_SIMPLIFIED_JOHNSON_COOK model, available in LS-DYNA [73], which accounts for strain-hardening and strain-rate effect on the current yield stress. Thermal softening and strain-based failure were neglected in the analyses. The material parameters, except the static yield strength, were taken from [8,17]. The rectangular plates were modelled as fully integrated shell elements using *ELEMENT_SHELL and *SECTION_SHELL keywords with ELFORM = 16 (free of hourglass modes) and three through-thickness integration points, NIP = 3, (to incorporate flexural effects). The uniform initial velocities were prescribed using the *INITIAL_VELOCITY_NODE keyword. Nodes on the plates' peripheries were restrained in all (including the rotational) degrees of freedom.

The peak displacement at the plate's centre was used to determine an appropriate element mesh density, which was then held fixed in subsequent analyses. The permanent displacement was determined by
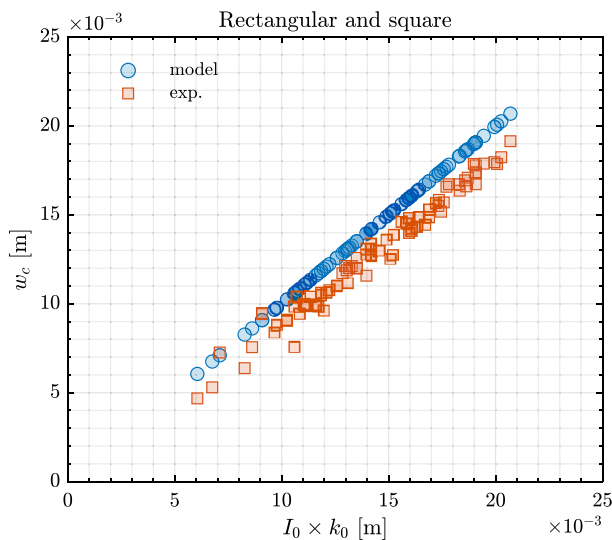
Fig. 6. Comparison of model predictions to experimental data [13] and LS-DYNA numerical results in terms of central residual displacement w_c of rectangular and square membranes under uniform impulse of total magnitude of I_0; k_0 is the membrane's parameter defined in Eq. (4.13).

averaging (through time integration) the displacement time history beyond the first peak over a small number of vibration cycles.

LS-DYNA results are compared to the experiments and the analytical predictions for the rectangular and square tests (separately) as shown in Fig. 7.

Aune and his team at SIMlab presented experimental and numerical studies on the response of thin plates under free-air blasts [62,63] and blasts produced in a shock tube facility [64]. Additional air-blast experiments are also reported by Spranghers et al. [65,66]. The rectangular plates are made of ductile materials (structural steel and aluminium). Some specimens are seen to respond impulsively and plastically. From the span-to-thickness ratios of some experiments and the intensity of the generated blast loads, the targets are thought to respond in membrane mode. Therefore, their experiments can, in general, be used to further assess the accuracy of the present model. However, few tests should be excluded from the validation analysis in which the plates: (1) experienced complete fractures, (2) had pre-formed cracks or holes, or (3) experienced a (counterintuitive) bifurcation or rebound buckling due to their ultra thinness when combined with low blast intensity. The validation of the model against the above experiments is not presented herein because the original works, cited above, did not provide quantitative information about the distribution of the blast-generated specific impulses, which the present model requires.

6.1.2. Discussion and model limitations

Figs. 6 and 7 exhibit a reasonable accuracy of the analytical model, Eq. (4.12), although the model accounts only for membrane behaviour, rigid-perfectly plastic material model, and idealised impulsive load.

However, as can be seen in the figures, the analytical model appears to be vertically offset when compared to the data. The offset is attributed to the fact that the model equation passes through the origin of w_c versus I_0, which is a shortcoming of the model since one expects a negative intercept on the w_c-axis (note that w_c is a plastic displacement).

From the other hand, it should be noted that Nurick et al. [13] measured (indirectly) the total impulse, and the actual specific impulse distribution (which is assumed uniform herein) was not reported. The slight discrepancy between the present model prediction and the experimental data could then be attributed to the implied lack of precise data.

Furthermore, the slight discrepancy can also be linked to the perfect plasticity assumption on the material behaviour. The model excludes strain-hardening and strain-rate effects, and for simplicity the static yield strength is taken as the perfectly plastic limit. However, many practical ductile materials exhibit various levels of yield enhancement due to these plastic effects. Heat-treated metals, e.g., typically possess substantial work-hardening where the current yield strength progresses gradually from the (less distinct) initial yield stress up to the ultimate strength that could be as twice as the initial yield strength [68]. A certain class of steel, which has been used in blast environments, exhibits different hardening-ductility characteristics depending on the material composition, heat-treatment, and manufacturing processes [64]. Idealising plates made of hardening materials as perfectly plastic would then result in overestimations of the responses under large dynamic loads. Therefore, it is important that such plastic characteristics are incorporated in computer numerical analyses since mathematical complexity is not a barrier.

The perfect plasticity assumption is adopted in the present work to obtain a "first-order approximation" model. Addition of the two mentioned effects into the model was found, by the authors, to lead to a nonlinear equation of motion. Therefore, the solution given by the present perfectly plastic model should be regarded as an upper-bound solution for structures made of materials that (in practice) deviate from the perfect plasticity behaviour.

If desirable, we propose that the yield strength to be used in the model might be adjusted (e.g. amplified) to compensate for large strain-hardening strengthening. For example, the *actual* area under the plastic part of the engineering stress–strain curve could be converted to a *rectangular* area, and by maintaining the ultimate strain, the characteristic (or effective) yield strength can then be determined. This procedure should give better predictions while maintain the upper-bound sense. However, in the foregoing validation work, the model is evaluated using the "static" yield strength because it was found to agree with the data.

A simplified study to assess the effect of work-hardening on the response of a single-degree-of-freedom (SDOF) due to blast-type loading is presented in Appendix C. Few representative numerical cases are given in which the ratios of the constant hardening moduli to elastic stiffness are in a range of practical values. Furthermore, a numerical parametric study using LS-DYNA of the effect of strain-hardening on the residual response of thin plates is also given in Appendix C; in addition, the corresponding predictions by the present analytical model are compared to LS-DYNA results.

The experiments in [62–66], discussed earlier, can be used to quantify the effect of neglecting the work-hardening in the model as some uniaxial tensile specimens show a significant presence of strain-hardening.

Finally, it should be re-emphasised that values of the material parameters, except the static yield strength, used in the LS-DYNA simulations are assumed. The source papers reported neither the Johnson–Cook (JC) parameters nor re-usable stress–strain data to enable identifications of the constitutive plastic parameters. For example, Nurick et al. [13] present the engineering stress–strain data at different strain rates. Using their data, it was attempted to obtain digitally converted true stress–strain curves and determine the material parameters by curve-fitting the data to JC model. However, this was not possible due to precision issues associated with the strain axis resolution. Thus, practical JC parameters (except the static yield strength) were adopted from [8,17], as mentioned already. Curry, in [17], pointed out that when quasi-static stress–strain data are fitted to JC model, the resulting static yield stress (A_{JC}) underestimates the value observed experimentally, due to the hardening power-law in JC model. Although, the used material parameters were found to give reasonable predictions when compared to the experiments. Example techniques to determine such parameters are explained in [17,74], and validated JC material parameters for some commonly used ductile materials are given in [8, 26,61,63,66].
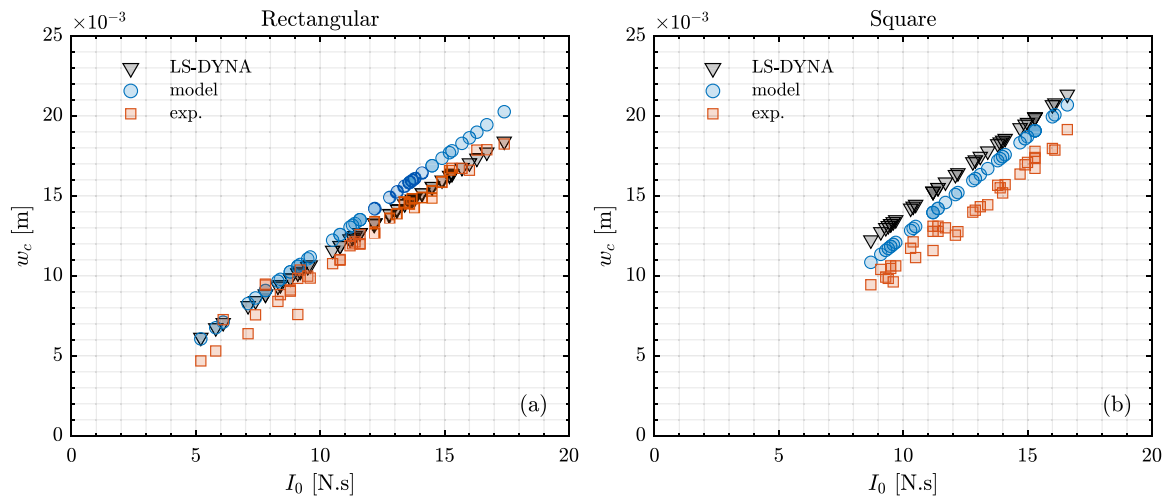
Fig. 7. Comparison of model predictions to experimental data [13] and LS-DYNA numerical results in terms of central residual displacement w_c of (a) rectangular and (b) square membranes under uniform impulse of total magnitude of I_0. LS-DYNA data are for permanent displacements. The data was separated for visual convenience.
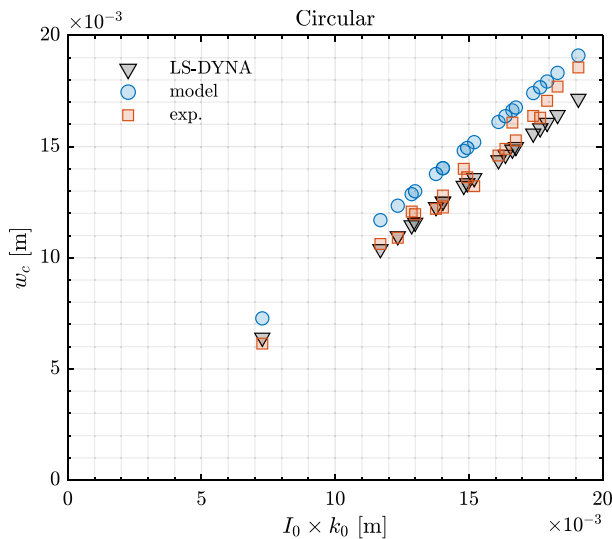

Fig. 8. Comparison of model predictions to experimental data [13] and LS-DYNA results in terms of central residual displacement w_c of circular membranes under uniform impulse of total magnitude of I_0; k_0 is the circular structural parameter defined in Eq. (5.10).

6.2. Circular model verification

6.2.1. Uniform impulse

In this section, we compare the predictions of the circular model for uniform specific impulse, as given by Eq. (5.9), to experimental data and numerical LS-DYNA predictions. Nurick, Martin, and Pearce [13], discussed in Section 6.1.1, also report experimental data for the permanent displacements of circular membranes of fixed diameters of 100 mm when subjected to uniform impulses of varying amplitudes. The membrane material properties and thickness are as described for the rectangular membrane, see Section 6.1.1. The data are compared to predictions from the model for the uniformly loaded circular membranes, Eq. (5.9). The characteristic yield strength σ_0 is taken as the static yield strength in [13]. The results are shown in Fig. 8.

In addition, LS-DYNA was used to replicate the tests of Nurick et al. [13] for the circular membrane case. Axisymmetric conditions were assumed in the simulations, and hence the problems were solved

using beam elements along the radial axis of the plates using *Elem-ent_Beam and *Section_Beam keywords with Elform = 8 and three through-thickness integration points, IR/QR = 3. With this set-up, it is unnecessary to specify the conditions at the axis of symmetry. Because the axisymmetric solver was utilised, the *Mat_Modified_Johnson_Cook model was used; it should be noted that the "modified" and "simplified" Johnson–Cook models differ in describing the strain-rate sensitivity. Again, applicable material parameters (except the static yield strength) were adopted from [8,17]. Motion is induced by a uniform initial velocity field calculated from the uniform specific impulse, and the periphery node was fully restrained. Finally, the central displacement was chosen to carry out mesh convergence study to determine the appropriate mesh density, which was then maintained throughout.

The finite element results for the permanent displacement are compared to the present analytical model and the experimental data of Nurick et al. [13], as shown in Fig. 8.

Gharababaei and Darvizeh [14] report results from 86 experiments on circular plates. The authors measured the central permanent displacements of steel, copper, and aluminium thin plates and the total impulses they were subjected to using a ballistic pendulum. All specimens had circular exposed areas with a fixed diameter of 100 mm. Among the experiments, 42 tests are assumed to generate spatially uniform specific impulse based on the following. The blast loads were generated by detonating thin (cylindrical) disks of C4 explosives located at a stand-off distance of 300 mm from the plates' centres for the 42 tests. The smallest scaled distance was Z = 1.12 m/kg$^{1/3}$, and a 9.5° angle of incidence at the plates' periphery was held constant for the tests. Furthermore, the authors used a rigid circular tube of equal diameter as that of the specimens to guide the propagation of the shock waves along its axis. Further details can be found in the original paper.

The predictions from the present model, Eq. (5.9), and LS-DYNA simulations are compared to the experimental data of Gharababaei and Darvizeh. Again, the static yield strengths reported in experiments are taken as the characteristic yield strengths in the model calculations. The data for the aluminium plates were excluded due to numerical difficulties in simulating their behaviour as the material is not strain-rate sensitive, and there is no available material data given in [14] regarding its strain-hardening parameters. The results are given in Fig. 9.

As shown in Fig. 9, the model does not accurately predict the experimental outcomes of Gharababaei and Darvizeh [14], in particular for $k_0 \times I_0$ larger than 0.03 m. The model overpredicts the permanent displacement by at most a factor of two.

Fig. 10 compares the model to data from LS-DYNA alone, which combines data already shown in Figs. 8 and 9. In the validation data
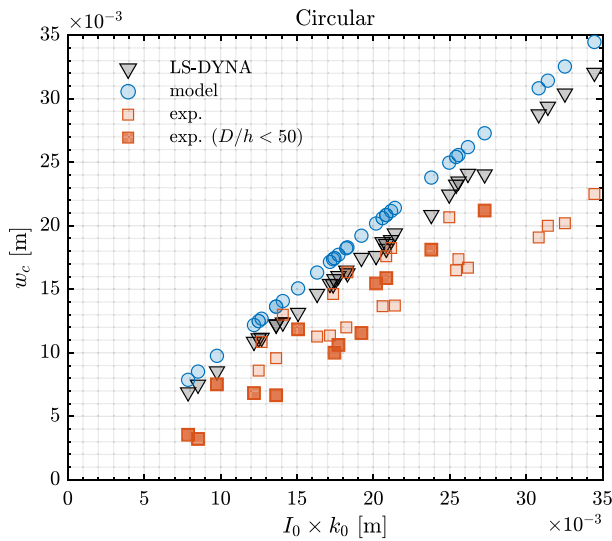
Fig. 9. Comparison of model predictions to experimental data [14] and LS-DYNA results in terms of central residual displacement w_c of circular membranes under uniform impulse. In [14], the total impulse I_0 was measured by ballistic pendulum; however, it was generated from thin disks of explosives with charge-to-target radius ratios of 0.2 and 0.30, but with a stand-off distance to plate's diameter ratio of 3.0. Experimental data for specimens with diameter-to-thickness ratio, (D/h), less than 50 are highlighted with filled red markers. k_0 is the circular structural parameter defined in Eq. (5.10).

Fig. 11. Comparison of model predictions to experimental data [15] in terms of central residual displacement w_c of circular membranes under uniform impulse of total magnitude of I_0. k_0 is the circular structural parameter defined in Eq. (5.10).
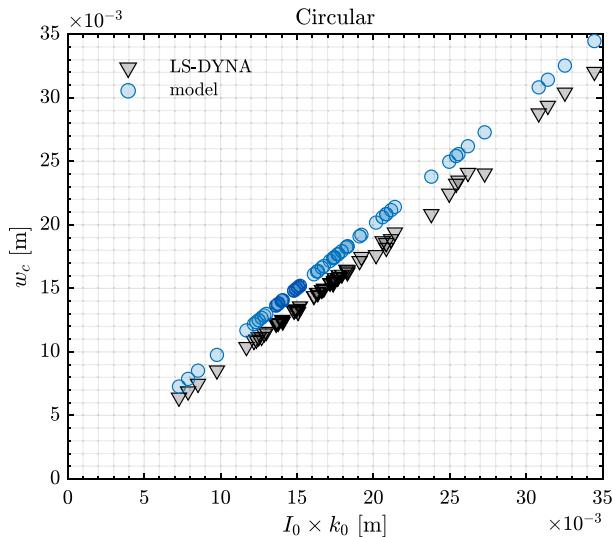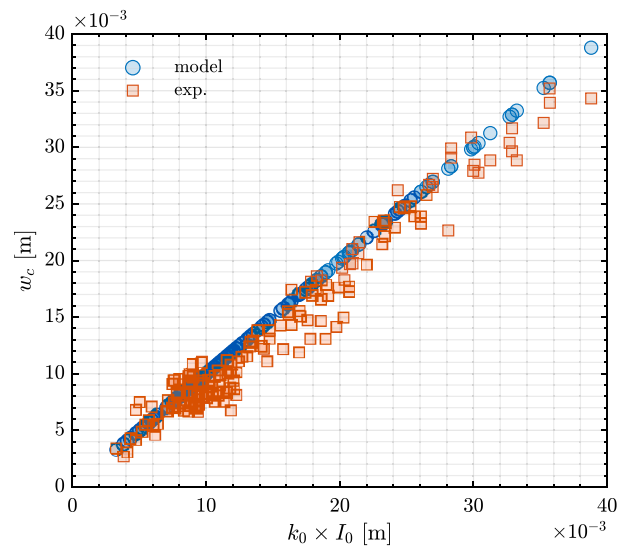

Fig. 10. Comparison of model predictions to results from LS-DYNA simulations corresponding to the experimental set-ups in [13,14] in terms of central residual displacement w_c of circular membranes under uniform impulse of total magnitude of I_0. Numerical material parameters (except the static yield strength) were taken from [8] for the steel plates. Notice that LS-DYNA simulations account for elasticity, strain-hardening, strain-rate sensitivity, bending and shear effects, which the present analytical model completely ignores. k_0 is the circular structural parameter defined in Eq. (5.10).

in Fig. 10, yield strength, plate thickness and density are variables in addition to the total impulse. As the model properly captures the trend of LS-DYNA predictions, it is concluded that the functional form of w_c in terms of these structural parameters is accurate.

Nurick, Gelman and Marshall [15] present additional 162 experiments on circular steel plates, of varying diameters, loaded with uniform impulses. All had 1.6 mm thickness and assumed density of 7850 kg/m^3. For plates with diameters 60, 80, 100, 120 mm, the corresponding static yield strengths were given as 251, 220, 270, 220

MPa, respectively. These specimens were clamped with sharp edges. Two additional sets of specimens with filleted clamping supports had diameters of 100 mm and yield strength of 251 MPa each. All data, including the total impulses and central residual displacements, are tabulated in Nurick et al. [15], and further details can be found there. Their data, excluding five tests for which displacements are not reported, are used to verify the circular membrane solution, Eq. (5.9), as shown in Fig. 11.

So far, the experimental tests used for the validation involve limited ranges of plates' thicknesses. To further assess the performance of the model under combined variations of total impulse and plate thickness in broader ranges, the input data presented in Rigby et al.'s [8] was used in additional LS-DYNA simulations. The set-ups are similar to those described earlier. From a sample simulation run, the central displacement time history is shown in Fig. 12. The results of the latter investigation are depicted in Fig. 13, which demonstrates the accuracy of the present model under varying plate thicknesses.

6.2.2. Discussion and limitations

The discussion and limitations presented in Section 6.1.2 for the rectangular case are also applicable to the validation of the uniform circular model against the experiments of Nurick et al. [13,15]. In general, the model slightly deviates from the experimentally observed measurements.

However, there is a pronounced discrepancy when comparing the uniform model to Gharababaei and Darvizeh's [14] data. This required a reappraisal of the model, the input data, and the testing set-up to trace the source of discrepancy. As previously discussed, the authors used a rigid tube as a blast wave guide that (when combined with the moderate stand-off distance) could produce wave reflection effects due to the interaction near the tube's wall. However, the assumption of uniformity of the impulse is ruled out. If the resulting specific impulse was indeed non-uniform, then according to [5,8], the displacement would then be even larger than that induced by a uniform impulse.

Although the model is built to predict membrane behaviour of thin plates, it performs better for the relatively thicker plates in [14] than it does for specimens with diameter-to-thickness ratios greater than 50. This can be seen in Fig. 9, in which the markers for thicker specimens are filled in red to highlight such observation. Furthermore, the trend of the experimental data deviates from the expected behaviour that moderately thicker plates are stiffer. This is because: (1) extra resisting
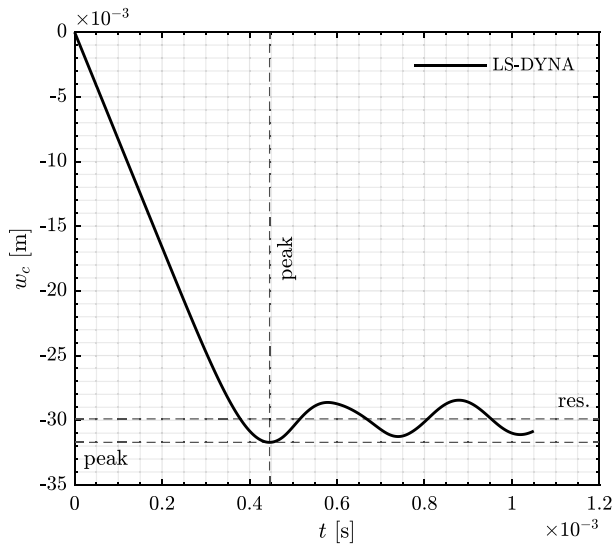
Fig. 12. Time history of the central displacement w_c from LS-DYNA simulation for a sample problem using input parameters given in [8]. Negative values on the ordinate y-axis correspond to downward displacements. It is seen that the resulting displacement is mainly plastic.
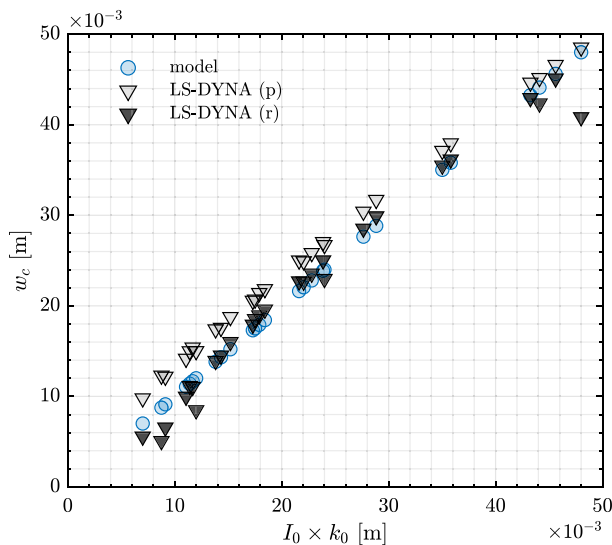

Fig. 13. Comparison of model predictions to LS-DYNA results in terms of central residual displacement w_c of circular membranes under uniform impulse of total magnitude of I_0. In the numerical simulations, input parameters were obtained from the parametric study in [8] to investigate the model performance for a wide range of plate's thickness. Peak (p) and residual (r) displacements from LS-DYNA analyses are shown.

modes are involved, i.e. bending and shear, that also contribute to absorb (or dissipate) the initial kinetic energy; and (2) due to increased mass per unit area, thicker plates attenuate the initial velocity generated by the (externally) imparted impulse according to Rigby et al.'s [8].

However, since an increase in the impulse leads to increase in initial velocity (for a given plate), the dynamic yield stress increases (due to strain-rate effects), which in turn would reduce the permanent displacement. Thus, the discrepancy between the model predictions and the experimental displacements for the range of larger impulses can be partly attributed to neglecting the strain-rate sensitivity of the yield strength and possibly, as discussed in Section 6.1.2, the work-hardening of the specimens (in particular made of copper).

Table 3
Comparison of the present model against the modified Nurick and Martin's model proposed by Yuen et al. [19].

Geometry:	α		β	
	Yuen et al.	Present	Yuen et al.	Present
Circular	0.241	0.281	0.298	0.0
Rectangular	0.253	$0.480 \times S_0(L_y/L_x)^{1/2}$	-0.158	0.0
Square	0.253	0.270	-0.158	0.0

Furthermore, similar to the discussion in Section 6.1.2, the authors in [14] measured the total impulse indirectly using a ballistic pendulum. Rigby et al. [55] pointed out that targets typically experience $\sim 67\%$ of the total impulses calculated from the ballistic pendulum measurements. Their conclusion can explain the observed discrepancy between the model predictions and Gharababaei and Darvizeh's [14] data.

6.3. Comparison of uniform circular and rectangular models to the modified Nurick and Martin model

Yuen et al. [19] proposed modifications to Nurick and Martin's [54] model. In their model, the normalised permanent displacement (i.e. displacement-thickness ratio), w_c/h, of circular or rectangular thin plates with exposed areas, A, is linearly related to the non-dimensional impulse, $\hat{\phi}$,

$$\hat{\phi} = \frac{I_0}{h^2\sqrt{\rho\sigma_0 A}},$$

by the following empirical relation, see [19],

$$\frac{w_c}{h} = \alpha\hat{\phi} + \beta$$

where α and β are correlation coefficients given in Yuen et al. [19] and presented in Table 3 for convenience. Note that we divided α (reported in Yuen et al. [19]) by $\sqrt{\pi}$ and 2, respectively, for the circular and rectangular models to unify the form of $\hat{\phi}$ for the two geometries, as given above.

Their empirical models were shown to reasonably predict the response of the thin plates compared to 699 (circular) and 356 (rectangular) experiments. Thus, it is of interest to compare the present model, developed herein, to their findings. For the present model, the coefficients α and β are obtained from the previously developed solutions by rewriting them in terms of $\hat{\phi}$.

The comparisons are summarised in Table 3. The values $S_0 = 0.5627$ and $\sqrt{L_y/L_x} = 1$ were used to calculate α for the square geometry using the expression of α for the rectangular model, given in Table 3. Note that β is zero for all cases of the present model. While Yuen et al.'s α and β are identical for the rectangular and square plates, the present model's α depends on the aspect ratio, L_y/L_x, (the parameter S_0 also depends on the aspect ratio). Since the value of β from Yuen et al. is small and will be multiplied by the plate's thickness to give a fraction of w_c, β can be neglected for our purpose of comparison. Overall, the present model overestimates the displacement by around 7∽17% (based on α) compared to the predictions of Yuen et al. [19].

From the comparisons of the present model against data from experiments and LS-DYNA simulations, presented in Sections 6.1.1 and 6.2.1, it is concluded in overall that the model is reasonably accurate in predicting the permanent displacements of rectangular and circular membranes under uniformly distributed specific impulses. The comparison of the uniform model to the already validated predictions of Nurick and Martin [54] and Yuen et al. [19], presented in this section, also supports this conclusion.

7. Limitations

Despite the relative accuracy of the present model, it has several shortcomings.

First, during the development of the equation of motions, the membrane is assumed to be already yielding as long as there is motion. That is, there is no rigid body motion. The whole membrane experiences (non-uniformly) distributed plasticity.

Second, "plastic" motion is assumed to be initiated by initial velocity, which is directly given by the imposed specific impulse. Hence, the model cannot determine the amount of impulse to be elastically absorbed. Therefore, any amount of given impulse leads immediately to an onset of "plastic" deformation. The model indicates that kinetic energy is at maximum at the initial time state, which gradually and monotonically decays as plasticity evolves. The model assumes complete removal of the external load (that induced the specific impulse) before motion, and hence the decreasing rate of kinetic energy is identical to the increasing rate of plastic work; the time history of plastic work is of an inverted form of the kinetic energy history.

Third, the yield strength is independent of the evolution of the membrane's motion. That is, enhancement (or hardening) of the yield stress due to strain-hardening and strain-rate sensitivity are not (correctly) incorporated. This is due to the perfect plasticity assumption, and a detailed discussion was given earlier in Section 6.1.2.

Fourth, the displacement components along the in-plane coordinates of the undeformed membrane are assumed negligible as compared to the out-of-plane component. In fact, the in-plane components are set identically to zero throughout. Hence, the longitudinal Green–Lagrange strains are merely due to the quadratic terms of the gradient of the out-of-plane displacement. This, in turn, leads to zero membrane strains at points where zero gradients occur, such as at the centre of a symmetrically loaded membrane. Experiments often show that this is not true; in fact, the peak membrane strains in uniformly and impulsively loaded membranes are located near their central regions. Despite this shortcoming, the model is able to predict thinning of the membrane near its restraints (i.e. where it is supported). This is directly due to the plastic incompressibility, which necessarily gives the transverse longitudinal strain as the negative of the sum of the other two longitudinal strains (which are always non-negative); thus, thickness shortens in strained regions.

Finally, the model focuses on thin plates subjected to extreme out-of-plane blast loads. The model excludes flexural and direct-shear mechanisms. The model should, then, be limited to thin plates with high span-to-thickness ratios and subjected to intense lateral forces. Therefore, the model can only predict failure in the form of thinning-induced splitting. Thus, the model does not apply to cases where direct shear failures near the supports occur. Note that as the load intensity becomes very low or the load duration increases significantly, the model is not suitable since elastic and flexural effects become important.

Attempts by the authors to incorporate as many sophistications as needed to replicate the actual behaviour of the studied membrane response would eventually lead to an incremental analysis of a nonlinear dynamic problem. We did not attempt to re-discover an already existing problem which can be tackled by existing techniques (e.g. FE analysis using LS-DYNA). Instead, we aimed to simplify the problem using overall observations that capture the "dominant" behaviour to ultimately obtain a model that rationally balances accuracy, simplicity, and efficiency.

Further justifications of the model's assumptions and the aim of the work were given earlier in Sections 1 and 2.

8. Summary and conclusions

Analytical solutions were developed to predict the profile and peak permanent displacement of thin plates under impulsive blast loads. The plates' materials were assumed rigid-perfectly plastic, obeying von Mises's yield criteria, and their motions were initiated from the blast-induced specific impulse. This problem set-up led to a monotonic deformation path, which was exploited in deriving the governing equation of motion systematically through the application of the extended Hamilton's principle. The equations of motion apply to thin plates deforming mainly in membrane modes and plastically. Although the obtained equations are general, solutions were given for two membrane geometries, rectangular and circular, by the modal decomposition technique. The modal decomposition was supplemented with sequential mode terminations, a strategy that is justified herein by Drucker's requirement of plastic work non-negativity.

The rectangular solution applies to any spatial distribution of specific impulses. A practical MATLAB code is proposed to efficiently compute the total modal impulses involved in the general solutions for non-uniform impulses. Moreover, a procedure to estimate the errors from truncating the infinite series in the solutions was discussed in connection to the concept of the upper bound kinetic energy of Rigby et al. [8]. The circular solution is restricted to axisymmetric specific impulses.

However, it was possible to provide simple closed-form solutions for the case of uniform specific impulse. The closed-form solutions of rectangular and circular thin plates were verified against experimental data in the literature and results from LS-DYNA simulations performed by the authors.

The present models for the rectangular and circular membranes were shown to be reasonably accurate in comparison to the experimental and numerical results. It should be emphasised that the models account only for simplified idealisations: an *impulsive* blast load, a *rigid-perfectly plastic* material behaviour, and a *membrane* mode of deformation. As a result, the obtained models are believed to be (already validated) simple and fast-running tools. Thus, they can be used by structural blast engineers for probabilistic-based analyses. Although the analytical models were compared against cases with uniform imparted impulsive loads, the general relations derived herein can readily model non-uniform impulsive loads.

CRediT authorship contribution statement

Saud A.E. Alotaibi: Formal analysis, Validation, Data curation, Writing – original draft, Visualization. **Samuel E. Rigby:** Conceptualization, Methodology, Supervision, Software, Writing – review & editing, Validation. **Maurizio Guadagnini:** Supervision, Methodology, Writing – review & editing. **Andrew Tyas:** Conceptualization, Methodology, Supervision, Resources.

Data availability

Data will be made available on request.

Appendix A. Assessment of error due to series truncation

Unless the specific impulse distribution identically matches the shape of a particular mode, the exact solution, as given by Eqs. (4.8) and (4.9), requires taking an infinite number of terms in the sum. However, in practice, a finite number of terms is used to approximate the solution within reasonable accuracy. An appropriate measure to evaluate the sufficiency of the approximation is the total kinetic energy. Suppose that the kinetic energy computed by including a finite number of modes is close to the "exact" kinetic energy, which is a strict upper bound due to the non-negativity of kinetic energies. Then, the discarded modes will be insignificant as their total contribution is bounded from above by the implied error (or difference). It is the *initial* kinetic energy that is referred to, which is

$$E_k = \int_0^{L_x} \int_0^{L_y} \frac{1}{2} \rho h \dot{w}_0^2 \, dy \, dx$$
$$= \frac{1}{2\rho h} \int_0^{L_x} \int_0^{L_y} i(x,y)^2 \, dy \, dx. \tag{A.1}$$

Again, this is taken as the "exact" kinetic energy at time $t = 0$, and it is termed the "upper bound kinetic energy" uptake in Tyas and Pope [5] and Rigby et al. [8].

Due to the assumption of deformation monotonicity, the total plastic work is associated with the total strain at the final time (as the problem is path-independent). That is, after $t \geq t_{1,1}$, the plastic work W_p^* is evaluated using the final displacement field, $w_p(x,y)$, and hence is given by

$$W_p^* = \frac{2}{\sqrt{3}} \sigma_0 h \int_0^{L_x} \int_0^{L_y} \left[\frac{1}{2} \left(\frac{\partial w_p}{\partial x} \right)^2 + \frac{1}{2} \left(\frac{\partial w_p}{\partial y} \right)^2 \right] dy \, dx. \tag{A.2}$$

By exploiting the modal orthogonality property and after some lengthy algebraic simplifications, the plastic work evaluates to

$$W_p^* = \frac{1}{2\rho h} \frac{4}{L_x L_y} \sum_{m,n=1}^{\infty} I_{mn}^2. \tag{A.3}$$

The above, Eq. (A.3), is precisely the expression for the (initial) kinetic energy if we would evaluate it by time differentiating the general solution $w(x,y,t)$, Eq. (4.1), then set $t = 0$, which confirms that the initial kinetic energy is converted into (plastic) internal energy.

Now, when the expressions of the exact initial kinetic energy, E_k, from Eq. (A.1), and the final plastic work, W_p^*, are set equal, the following condition, known as Parseval's formula [75], is obtained

$$\sum_{m,n=1}^{\infty} I_{mn}^2 = \frac{L_x L_y}{4} \int_0^{L_x} \int_0^{L_y} i(x,y)^2 \, dy \, dx = \|\phi_{mn}\|^2 \cdot \|i\|^2 \tag{A.4}$$

where $\|f(x,y)\| = \sqrt{\int_A f(x,y)^2 \, dA}$, is the norm of a function f, and $\|\phi_{mn}\|$ is $\sqrt{(L_x L_y / 4)}$.

Therefore,

$$\sum_{m,n=1}^{\infty} I_{mn}^2 = \left(\frac{I_k}{2} \right)^2 \tag{A.5}$$

in which I_k is the energy-equivalent impulse due to Rigby et al. [8], which, for a rectangular target with loaded area $A = L_x L_y$, is given by

$$I_k = \sqrt{A \int_A i(x,y)^2 \, dA} \tag{A.6}$$
$$= \sqrt{A} \times \|i\|.$$

It should be noted that in [8], I_k was derived directly from the physical problem using equivalency between kinetic energies due to non-uniform and uniform specific impulses.

Now, defining an angular parameter, which measures how much the actual specific impulse field is along the direction of one particular mode (in the inner product sense), by

$$\cos \theta_{mn} = \frac{2 I_{mn}}{I_k} \tag{A.7}$$

then, one reaches the following general condition

$$\sum_{m,n=1}^{\infty} \cos^2 \theta_{mn} = 1. \tag{A.8}$$

It is vital to recognise that there is no single component in the infinite series above, Eq. (A.8), with a magnitude larger than unity since each term is always positive while the right-hand side is one. Hence, if one term is identically one, then all other terms must vanish, which is the situation when the specific impulse field matches the shape of the surviving (or resonating) mode.

Finally, if only a finite number of terms is used to calculate w_p or w_c, then it is sufficient to verify that the sum of $\cos^2 \theta_{mn}$, for those modes included, is close to unity (from below). In other words, the error, ϵ, due to truncation at $m = M$ and $n = N$, can be estimated as

$$\epsilon_{MN} = 1 - \sum_{m,n=1}^{M,N} \cos^2 \theta_{mn} \equiv \sum_{M,N}^{\infty} \cos^2 \theta_{mn}. \tag{A.9}$$

The quantity $\cos \theta_{mn}$, on its own, gives the absolute *physical* importance of the (m,n)th mode in relation to all other modes since it compares the modal energy (through I_{mn}) to the strict upper bound kinetic energy, E_k, (through I_k).

Appendix B. A practical method to compute I_{mn}

For smoothly varying distribution of specific impulse, I_{mn} decreases as m and n increase due to cancellations associated with high spatial oscillations. Thus, practically a finite number of modes suffices to estimate the displacement accurately.

In the expression for w_c, instead of carrying out the numerical integrations directly by the trapezoidal rule, it is observed that the two-dimensional Fast Fourier Transform (FFT) could be utilised to reduce the computational time. However, according to the form of I_{mn}, the specific impulse distribution should be slightly manipulated first. The procedure is quite simple to derive, and it is briefly described below and followed by a practical MATLAB code for the implementation.

From the actual specific impulse, $i(x,y)$, defined on the actual membrane that spans the domain $[0, L_x] \times [0, L_y]$, construct a fictitious specific impulse $i^*(x,y)$ that covers an extended rectangular region $[-L_x, L_x] \times [-L_y, L_y]$, which is defined as

$$i^*(x,y) = \begin{cases} i(x,y), & (x,y) \in [0, L_x] \times [0, L_y], \\ -i(-x,y), & (x,y) \in [-L_x, 0] \times [0, L_y], \\ -i(x,-y), & (x,y) \in [0, L_x] \times [-L_y, 0], \\ i(-x,-y), & (x,y) \in [-L_x, 0] \times [-L_y, 0]. \end{cases} \tag{B.1}$$

Now, the real components of the two-dimensional discrete Fourier transform of $i^*(x,y)$ is denoted by b_{mn} and given by

$$b_{mn} = \frac{1}{L_x L_y} \int_{-L_x}^{L_x} \int_{-L_y}^{L_y} i^*(x,y) \sin\left(\frac{2 m\pi x}{2 L_x} \right) \sin\left(\frac{2 n\pi y}{2 L_y} \right) dy \, dx. \tag{B.2}$$

It is important to note that the x-interval is $2L_x$ and that along y is $2L_y$.

Next, $b_{mn} = b(m,n)$ is related to the complex Fourier coefficients by

$$b_{mn} = -c(m,n) + c(-m,n) + c(m,-n) - c(-m,-n) \tag{B.3}$$

where m and n are indices corresponding to positive integers, and $-m$ and $-n$ are indices corresponding to negative integers. Then, using the piecewise definition of $i^*(x,y)$, it can be shown that b_{mn} reads

$$b_{mn} = \frac{4}{L_x L_y} \int_0^{L_x} \int_0^{L_y} i(x,y) \sin\left(\frac{m\pi x}{L_x} \right) \sin\left(\frac{n\pi y}{L_y} \right) dy \, dx$$
$$= \frac{4 I_{mn}}{L_x L_y}. \tag{B.4}$$

Finally,

$$I_{mn} = \frac{L_x L_y}{4} \left[-c(m,n) + c(-m,n) + c(m,-n) - c(-m,-n) \right]. \tag{B.5}$$

The values of $c(m,n)$, $c(-m,n)$, $c(m,-n)$, and $c(-m,-n)$ are the standard outputs of an FFT, to within a constant multiplier. FFT gives the amplitudes of the modes, e.g. $c(0,0)$ reflects the amplitude of the mode associated with $m = 0$ and $n = 0$. In MATLAB, this is achieved using the built-in function fft2(). Note that in MATLAB, the output sorts the number of modes in each direction in a special order: first, the zeroth mode (which we do not need), followed by positive modes in ascending order, and lastly negative modes in descending order.

The specific procedure to be implemented in MATLAB is what follows. Let the actual specific impulse, $i(x, y)$, be stored in 2D array I. Further, let the plate lengths along x and y be Lx and Ly, respectively.

Then, denote $i^*(x, y)$ by Istar, which can easily be formed in MATLAB using the built-in function flip(). Finally, say the total modal impulse, I_{mn}, will be stored in the array Imn and be evaluated using FFT. The MATLAB procedure is given in Script 1.

```
%% start of script
% I =specific impulse matrix (2D array)...
% rows of I --> variation along x
% cols of I --> variation along y

Istar=[flip(flip(I,1),2),-flip(I,1);-flip(I,2),I];

C0=fft2(Istar);
C0=real(C0);
C0=1/(numel(Istar))*C0; %undo multiplier
C1=C0(2:end,2:end); %skip zeroth mode
B=zeros(ceil((size(C1)-1)/2));

for i=1:size(B,1)
    for j=1:size(B,2)
        B(i,j) = -C1(i,j)+C1(end-i+1,j)+C1(i,end-j+1)-C1(end-i+1,end-j+1);
    end
end

Imn=Lx*Ly*B/4;

% Imn stores total modal impulses, Imn.
% Use this directly in expressions for displacement w_p or w_c.
%% end of script.
```

Script 1: MATLAB script to compute I_{mn} efficiently using FFT

By comparing the results (not shown herein) from computing I_{mn} via the trapezoidal rule for a large number of modes in each direction to those using the FFT, the observations are FFT is superiorly efficient and very reasonably accurate. Hence, the use of FFT to evaluate I_{mn} is recommended. This computational strategy is rarely pointed out in the literature as an efficient method to compute the modal amplitudes appearing in the displacement response of plates.

Appendix C. Effect of work-hardening on the response of an SDOF and plate

C.1. Forced response - SDOF

In this section, an assessment of the effect of work-hardening is presented based on the response of a single-degree-of-freedom (SDOF). The system consists of a mass m, a massless spring with resistance R, and an applied dynamic force, and its general equation of motion is

$$m\ddot{x} + R = F$$

For simplicity, we are concerned with motion up to a half cycle beyond the first maximum response. The SDOF is assumed as initially at rest.

The resistance R is of bilinear form during loading and has an elastic unloading

$$R = \begin{cases} kx & t \leq t_{y,0}, \\ R_{y,0} + H(x - x_{y,0}) & t_{y,0} \leq t \leq t_m, \\ R_{y,0} + H(x_m - x_{y,0}) + k(x - x_m) & t_m \leq t \end{cases}$$
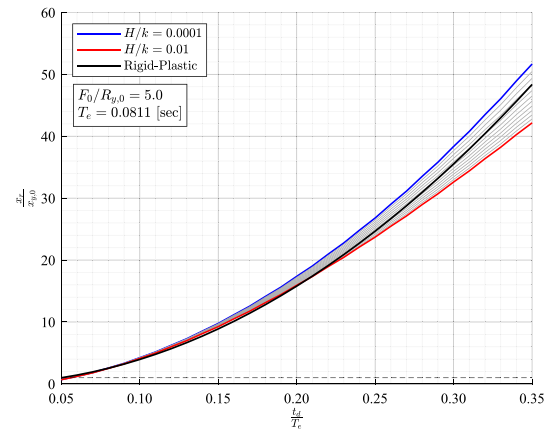

Fig. C.1. Normalised residual displacement $x_r/x_{y,0}$ of elasto-plastic SDOF as function of the ratios of load duration to elastic period t_d/T_e and hardening modulus to elastic stiffness $\frac{H}{k}$. The grey curves are for intermediate ratios of H/k, which are bounded by the values of the blue and red curves.

where k and H are the elastic stiffness and the hardening modulus; $R_{y,0}$, $x_{y,0}$, and $t_{y,0}$ are the initial yield force, the corresponding yield displacement, and the time at which first yielding occurs. The maximum displacement is x_m. The last expression for R describes the elastic unloading for sufficiently small-time interval after $t = t_m$.

The applied force F is assumed to be a rectangular pulse with amplitude F_0 and duration t_d.

The elasto-plastic response of the SDOF was solved numerically using an explicit time integration scheme. The solution is terminated after completing a half cycle from the first occurrence of maximum displacement (i.e. after sufficient time during the elastic unloading/rebound), in order to obtain sufficient response to compute the residual displacement, x_r.

We considered the following input data. The elastic period $T_e = 2\pi\sqrt{m/k}$ is 0.0811 s. The ratio of the external force to the initial yield limit $F_0/R_{y,0}$ is 5.0. The ratio of load duration to the elastic period t_d/T_e and the ratio of hardening modulus to elastic stiffness H/k are varied independently; some practical ratios of H/k are considered. The results for the normalised residual displacement $x_r/x_{y,0}$ are given in Fig. C.1.

The Rigid-plastic response of the SDOF is obtained by substituting $R = R_{y,0}$ in the equation of motion, which is valid since $F_0 > R_{y,0}$, and hence it is expected that $\dot{x} \geq 0$. Therefore, the maximum displacement is

$$x_{m,rp} = x_{t_d} + \dot{x}_{t_d}(t_m - t_d) - \frac{R_{y,0}}{2m}(t_m - t_d)^2$$

where,

$$x_{t_d} = \left(\frac{F_0 - R_{y,0}}{2m}\right)t_d^2, \tag{C.1}$$

$$\dot{x}_{t_d} = \frac{F_0 t_d}{m} - \frac{R_{y,0} t_d}{m}, \tag{C.2}$$

$$t_m = \frac{\dot{x}_{t_d}}{\left(\frac{R_{y,0}}{m}\right)} + t_d \tag{C.3}$$

The maximum rigid-perfectly plastic displacement $x_{m,rp}$ is plotted in Fig. C.1 as a function of the ratio of load duration to elastic period t_d/T_e and compared to the residual displacement of the elasto-plastic problem.

It can be seen, from the figure, that the rigid-perfectly plastic solution gives reliable predictions as compared to the elasto-plastic solution with various work-hardening, in particular as the load duration to elastic period ratio t_d/T_e becomes very small. In Fig. C.1, the difference between the responses for the rigid-perfectly plastic (black) and elasto-plastic with $H/k = 0.0001$ (blue) is attributed to elastic deformations

of the elasto-plastic SDOF. Such difference should decrease as the external force to initial yield limit ($F_0/R_{y,0}$) increases while small t_d is maintained.

C.2. Impulsive response - SDOF

In this section, we present additional assessment of the effect of work-hardening on the response of the same SDOF as in the previous section. However, we consider the system where the external force is absent and assume the response to be driven by initial velocity. The initial displacement is assumed zero.

We consider the initial velocity, $\dot{x}_0$, to be large enough to cause initial yielding.

Denoting the time of initial yielding by $t_{y,0}$, the response for ($0 \leq t \leq t_{y,0}$) is governed by $m\ddot{x} + kx = 0$ with initial conditions $x_0 = 0$ and $\dot{x}_0 > 0$. The response is

$$\omega_e = \sqrt{\frac{k}{m}},$$
$$x(t) = \frac{\dot{x}_0}{\omega_e} \sin(\omega_e t)$$

From which, the state at $t = t_{y,0}$ is

$$x_{y,0} = \frac{R_{y,0}}{k},$$
$$t_{y,0} = \frac{\sin^{-1}\left(\frac{x_{y,0}\omega_e}{\dot{x}_0}\right)}{\omega_e},$$
$$\dot{x}_{y,0} = \dot{x}_0 \cos(\omega_e t_{y,0})$$

Denoting the time at maximum response (i.e. just prior to elastic unloading) by t_m, the response for $(t_{y,0} \leq t \leq t_m)$ is governed by $m\ddot{x} + R_{y,0} + H(x - x_{y,0}) = 0$ with initial conditions $x(t_{y,0}) = x_{y,0}$ and $\dot{x}(t_{y,0}) = \dot{x}_{y,0}$. The response is

$$\omega_H = \sqrt{\frac{H}{m}},$$
$$x(t) = x_{y,0}\cos\left[\omega_H\left(t - t_{y,0}\right)\right] + \frac{\dot{x}_{y,0}}{\omega_H}\sin\left[\omega_H\left(t - t_{y,0}\right)\right] +$$
$$(-1)\left(\frac{R_{y,0} - Hx_{y,0}}{H}\right)\left\{1 - \cos\left[\omega_H\left(t - t_{y,0}\right)\right]\right\}.$$

By definition t_m is the time when velocity becomes zero for the first time, i.e. $\dot{x}(t_m) = 0$. From which, the state at $t = t_m$ is

$$\beta = \tan^{-1}\left[\frac{\dot{x}_{y,0}}{\omega_H x_{y,0} + \left(\frac{R_{y,0} + Hx_{y,0}}{m\omega_H}\right)}\right],$$
$$t_m = \frac{\beta}{\omega_H} + t_{y,0},$$
$$x_m = x_{y,0}\cos(\beta) + \frac{\dot{x}_{y,0}}{\omega_H}\sin(\beta) - \left(\frac{R_{y,0} - Hx_{y,0}}{H}\right)[1 - \cos(\beta)].$$

For $(t \geq t_m)$, the response is an elastic rebound, which is governed by $m\ddot{x} + R_{y,0} + H(x_m - x_{y,0}) + k(x - x_m) = 0$, with initial conditions $x(t_m) = x_m$ and $\dot{x}(t_m) = 0$. The rebound response, for $t \geq t_m$, is

$$x(t) = x_m\cos\left[\omega_e(t - t_m)\right] +$$
$$(-1)\left(\frac{R_{y,0} + H(x_m - x_{y,0}) - kx_m}{k}\right)\left\{1 - \cos\left[\omega_e(t - t_m)\right]\right\}.$$

The residual (plastic) displacement, x_r, is obtained from the above rebound solution when the vibration terms (i.e. the cosine terms) are eliminated. With the elastic period

$$T_e = 2\pi\sqrt{\frac{m}{k}}$$

the residual displacement is

$$x_r = \frac{2}{T_e}\int_{t_m}^{t_m + \frac{T_e}{2}} x(t)\, dt$$

which simplifies to

$$x_r = -\frac{\left[R_{y,0} + H(x_m - x_{y,0}) - kx_m\right]}{k}$$

The initial kinetic energy, $E_{k,0}$, of the SDOF is

$$E_{k,0} = \frac{1}{2}m\dot{x}_0^2$$

and, the maximum (initial) elastic energy, $E_{e,m}$, is

$$E_{e,m} = \frac{1}{2}k x_{y,0}^2$$

For a given ratio of $E_{k,0}/E_{e,m}$ and a ratio of H/k, one can study the response in terms of ratio of maximum (or residual) displacement x_m (or x_r) to the initial yield displacement $x_{y,0}$. This gives direct assessment of the influence of work-hardening.

The rigid-perfectly plastic solution is characterised by the maximum response time $t_{m,rp}$ (when velocity reaches, and subsequently held constant at, zero) and the corresponding maximum displacement $x_{m,rp}$. These are defined by

$$t_{m,rp} = \frac{\dot{x}_0}{\left(\frac{R_{y,0}}{m}\right)},$$
$$x_{m,rp} = \dot{x}_0 t_{m,rp} - \frac{1}{2}\frac{R_{y,0}}{m}t_{m,rp}^2$$

The rigid-perfectly plastic response $x_{m,rp}$ can be compared to the response of the elasto-plastic with hardening solutions, the maximum x_m or residual x_r displacements, to assess the effects of both work-hardening and elasticity.

We consider a particular case for which the ratio of initial kinetic energy to maximum elastic energy is large, $\frac{E_{k,0}}{E_{e,m}} = 9.0$. The elastic period is $T_e = 0.0811$ s. Also, the ratio of the hardening modulus to the elastic stiffness H/k is taken as (0.01). The comparison of the time history responses of the elasto-plastic with hardening SDOF and the corresponding rigid-perfectly plastic SDOF is shown for the present case in Fig. C.2. The displacement x is normalised by $x_{y,0}$, and the time axis is normalised by t_y. The figure indicates that the rigid-perfectly plastic solution is suitable and highly efficient for response of the SDOF for the considered ratio of $E_{k,0}/E_{e,m} = 9.0$.

As a second example, we consider a problem with $E_{k,0}/E_{e,m} = 25.0$, $T_e = 0.1147$ s, and $H/k = 0.002$. The responses from the elasto-plastic with hardening model and the rigid-perfectly plastic model are compared in Fig. C.3.

C.3. Plate response - LS-DYNA

In this section, results from LS-DYNA simulations are presented to assess the influence of work-hardening on the response of a ductile thin plate loaded by a uniform impulse.

Flexural, shear, and membrane effects are all considered. Furthermore, a general elasto-plastic material behaviour is adopted. Plasticity follows a von-Mises yield function in which the yielding stress is given by Johnson–Cook (JC) model. In this study, the hardening saturation stress B is varied while all other material (and geometry and loading) parameters fixed.

The plate is impulsively loaded using a prescribed uniform initial transverse velocity $\dot{w}_0$

$$\dot{w}_0 = \frac{i_0}{\rho h}$$

where the uniform specific impulse, density, and uniform thickness are denoted by i_0, ρ, and h.
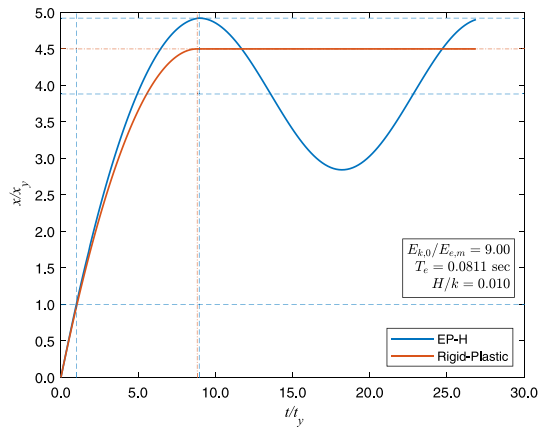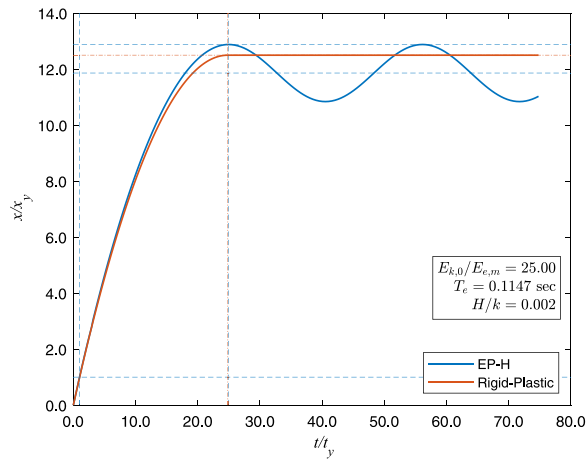
Fig. C.2. Normalised displacement $x(t)/x_{y,0}$ of elasto-plastic SDOF (with work-hardening) as function of normalised time $t/t_{y,0}$; hardening modulus to elastic stiffness ratio is $H/k = 0.01$. The response is for an impulsively loaded SDOF, i.e. with nonzero initial velocity and zero external force. The initial kinetic energy $\left(E_{k,0} = 1/2\, m\, \dot{x}_0^2\right)$ is nine times larger than the maximum elastic energy $\left(E_{e,m} = 1/2\, k\, x_y^2\right)$. Horizontal (blue) dashed lines are drawn at $x_{y,0}$, x_r, and x_m for the elasto-plastic response, and the additional (red) dashed line corresponds to $x_{m,rp}$ for the rigid-plastic response.

Fig. C.3. Normalised displacement $x(t)/x_{y,0}$ of elasto-plastic SDOF (with work-hardening) as function of normalised time $t/t_{y,0}$; hardening modulus to elastic stiffness ratio is $H/k = 0.002$. The response is for an impulsively loaded SDOF, i.e. with non-zero initial velocity and zero external force. The initial kinetic energy $\left(E_{k,0} = 1/2\, m\, \dot{x}_0^2\right)$ is 25 times larger than the maximum elastic energy $\left(E_{e,m} = 1/2\, k\, x_y^2\right)$. Horizontal (blue) dashed lines are drawn at $x_{y,0}$, x_r, and x_m for the elasto-plastic response, and the additional (red) dashed line corresponds to $x_{m,rp}$ for the rigid-plastic response.

According to JC model without Voce's hardening, the current yield stress σ_y is influenced by current effective plastic strain ε_{eff}, the instantaneous effective plastic strain rate $\dot{\varepsilon}_{\text{eff}}$, and the absolute temperature T using

$$\sigma_y = \left(A + B\, \varepsilon_{\text{eff}}^n\right) \left[1 + \left(\frac{\dot{\varepsilon}_{\text{eff}}}{\dot{\varepsilon}_0}\right)\right]^c \left(1 - T^{*m}\right)$$

where T^* is

$$T^* = \frac{T - T_r}{T_m - T_r}$$

in which T_m and T_r are the (absolute) melting and room temperatures.

B and n are power-law hardening parameters, c is a strain-rate sensitivity parameter. A is the initial quasi-static yield stress at the threshold strain rate $\dot{\varepsilon}_0$. Note that n is typically in the range $0 \leq n \leq 1$, and then B could be regarded as an increase in σ_y (from A) due to strain-hardening. A further strengthening in the strain-hardened σ_y occurs at high strain

Table C.4
JC material parameters.

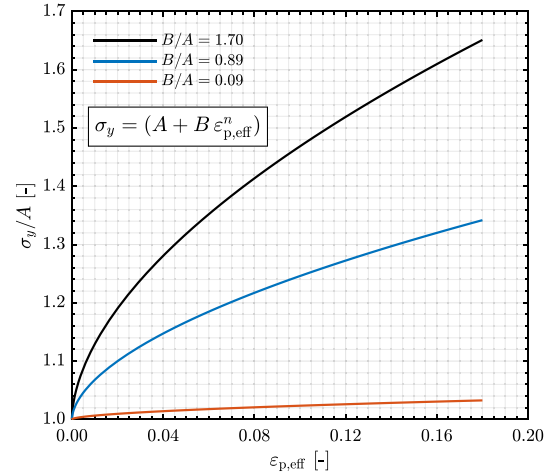| Parameter	Value	Unit
E	206×10^9	Pa
ρ	7830	kg/m³
v	0.29	–
A	296×10^6	Pa
n	0.5597	–
m	0	–
c	0.032	–
$\dot{\varepsilon}_0$	1.4×10^{-6}	1/s

Fig. C.4. Variation of JC current yield stress σ_y versus effective (von-Mises) plastic strain $\varepsilon_{\text{p,eff}}$ at the quasi-static plastic strain rate $\dot{\varepsilon}_0$. Curves correspond to different amount of strain-hardening in terms of B/A ratio.

rates. On the other hand, two softening mechanisms (thermal softening when m is non-zero and/or damage-induced softening) can lower σ_y. We assume that softening is absent for simplicity (i.e. $m = 0$ and damage threshold $= \infty$).

In the study, we considered the material input values as shown in Table C.4. Three values of B as multiples of A are considered. In particular, we consider ratios of B/A of 1.7, 0.89, and 0.05. These ratios correspond to the (true) yield stress-effective plastic strain curves in Fig. C.4.

The other input parameters are the following. The plate is square with a side length of 0.089 m and thickness of 1.6 mm. Additionally, a total impulse of −16.1 N m. is applied uniformly to the plate to give a uniform initial transverse velocity of −162.24 m/s. The input values correspond to the square plate tests of Nurick et al. cited and discussed in Section 4.2. All boundary nodes are restrained in all translational and rotational degrees of freedom. A fine element mesh is selected. The plate is modelled with two-dimensional shell elements using ELFORM = 7 (selectively-reduced integrated Hughes–Liu co-rotational formulation) and 10 Gauss integration points to better represent the extent of plasticity through the plate's thickness.

Nodal, element, and energy databases are requested with fine sampling rates. The transverse (z-) displacement and energy histories are post-processed in MATLAB. The residual displacement is computed by time integration averaging beyond the first peak response.

The history results obtained from LS-DYNA for the three ratios of B/A are compared to the predictions of the present model. Namely, the displacements at the plate's centre, the time to maximum response, and the evolution of different energies are analysed. In the model predictions, the characteristic yield strength σ_0 is taken as the static yield strength A.

The results are shown in Figs. C.5–C.8. It can be concluded that the higher the degree of strain-hardening the smaller the peak and residual
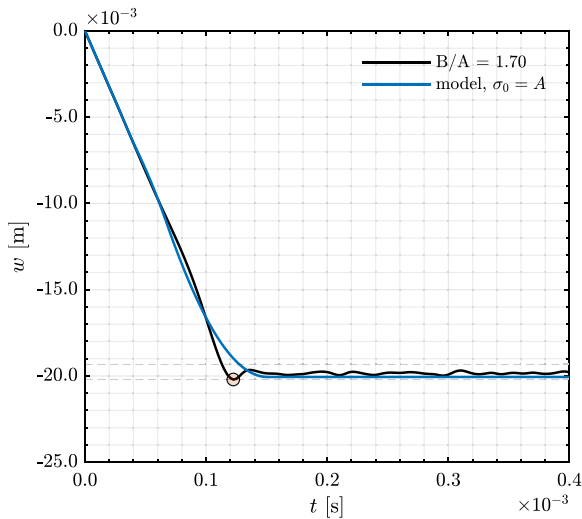
Fig. C.5. Central transverse displacement w time history from LS-DYNA simulation (for $B/A = 1.7$) and the corresponding model prediction.
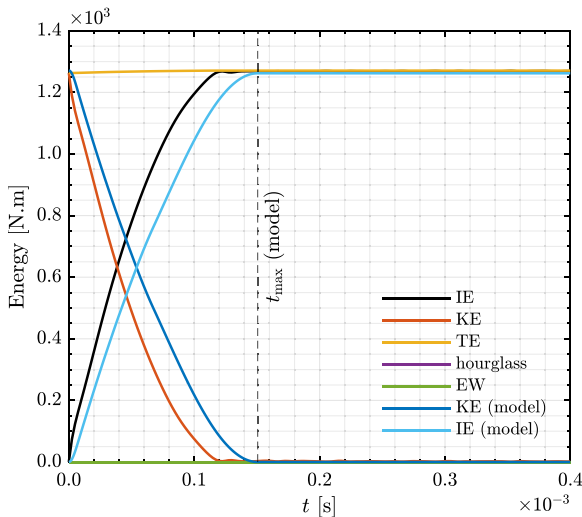

Fig. C.7. Effect of the degree of strain-hardening (in terms of B/A ratio) on the transient and residual central displacements from LS-DYNA. The model prediction assumes $\sigma_0 = A$.

Fig. C.6. Histories of global energies from LS-DYNA (for $B/A = 1.7$), and the corresponding kinetic (KE) and plastic internal (IE) energies predicted by the model. From LS-DYNA, the internal (IE), kinetic (KE), total (TE), and hourglass energies and external work (EW) are shown. The maximum response time t_{max} predicted by the model is shown as a vertical dashed line.

Fig. C.8. LS-DYNA maximum (peak) and residual (res.) displacements at the plate's centre as functions of the degree of hardening (in terms of B/A).

displacements are, as clearly depicted in Figs. C.7 and C.8. In addition, Figs. C.5–C.7 indicate that the model predictions capture both the time evolution of residual displacement and internal and kineitic energies, in particular as compared to the case with the largest B/A ratio.

References

[1] Rigby SE, Knighton R, Clarke SD, Tyas A. Reflected near-field blast pressure measurements using high speed video. Exp Mech 2020;60(7):875–88. http://dx.doi.org/10.1007/s11340-020-00615-3.

[2] Rigby SE, Tyas A, Clarke SD, Fay SD, Reay JJ, Warren JA, Gant M, Elgy I. Observations from preliminary experiments on spatial and temporal pressure measurements from near-field free air explosions. Int J Prot Struct 2015;6(2):175–90. http://dx.doi.org/10.1260/2041-4196.6.2.175.

[3] Tyas A. Blast loading from high explosive detonation: What we know and don't know. In: 13th int. conf. shock impact loads struct. SILOS 2019, 14-15 December 2019, Guangzhou, China, no. December. Guangzhou, China; 2019, p. 65–76.

[4] Tyas A. Experimental measurement of pressure loading from near-field blast events: Techniques, findings and future challenges. Proceedings 2018;2(8). http:
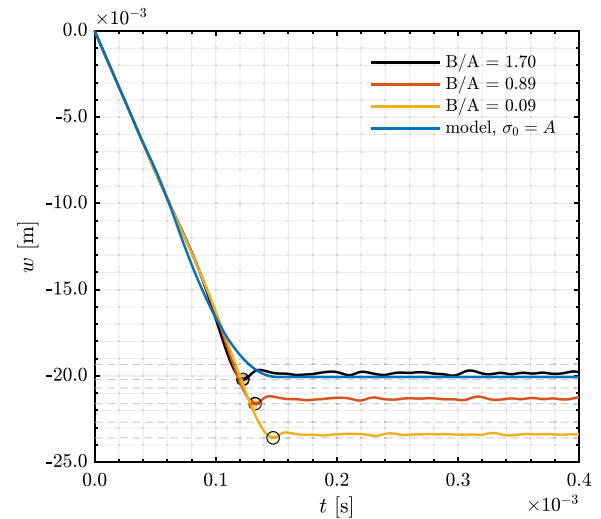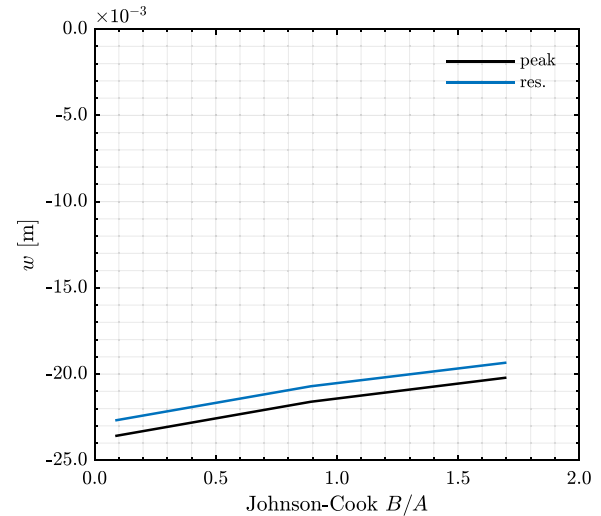
//dx.doi.org/10.3390/ICEM18-05364, URL https://www.mdpi.com/2504-3900/2/8/471.

[5] Tyas A, Pope DJ. The energy take-up of panels subjected to near-field blast loading. Int Conf Response Struct Extrem. Load. 2003;1(C).

[6] Jones N. Inelastic response of structures due to large impact and blast loadings. J Strain Anal Eng Des 2010;45(6):451–64. http://dx.doi.org/10.1243/03093247JSA611, URL https://journals-sagepub-com.sheffield.idm.oclc.org/doi/abs/10.1243/03093247JSA611.

[7] U.S. Army CoE. Structures to resist the effects of accidental explosions UFC 3-340-02. In: Unified facil. criteria 3-340-02. Tech. rep., U.S. Army Corps of Engineers; 2008, p. 1796, URL http://dod.wbdg.org/.

[8] Rigby SE, Akintaro OI, Fuller BJ, Tyas A, Curry RJ, Langdon GS, Pope DJ. Predicting the response of plates subjected to near-field explosions using an energy equivalent impulse. Int J Impact Eng 2019;128(January):24–36. http://dx.doi.org/10.1016/j.ijimpeng.2019.01.014, URL https://doi.org/10.1016/j.ijimpeng.2019.01.014.

[9] Reddy JN. Energy principles and variational methods in applied mechanics. John Wiley & Sons, Inc.; 2002, p. 592. http://dx.doi.org/10.1016/0307-904x(85)90131-3.

[10] Washizu K. Variational methods in elasticity and plasticity. Int. ser. monogr. aeronaut. astronaut. div. I solid struct. mech., 2nd ed.. Vol. 9, (2):Exeter, Great Britain: Pergamon Press; 1975, p. 70–1. http://dx.doi.org/10.1002/zamm.19840640121.

[11] Drucker DC. A definition of stable inelastic material. Tech. rep., Providence, Rhode Island: Division of Engineering, Brown University; 1957, p. 23, URL https://apps.dtic.mil/sti/pdfs/AD0143756.pdf.

[12] Drucker DC. Variational principles in the mathematical theory of plasticity. Tech. rep., Providence, R. I.: DIVISION OF APPLIED MATHEMATICS, BROWN UNIVERSITY; 1956, p. 24.

[13] Nurick GN, Pearce HT, Martin JB. The deformation of thin plates subjected to impulsive loading. In: Bevilacqua L, Feijno R, Valid R, editors. Inelast. behav. plates shells iutam symp. Rio de Janeiro. Rio de Janeiro; 1985, p. 597–616. http://dx.doi.org/10.1007/978-3-642-82776-1_29.

[14] Gharababaei H, Darvizeh A. Experimental and analytical investigation of large deformation of thin circular plates subjected to localized and uniform impulsive loading. Mech Based Des Struct Mach 2010;38(2):171–89. http://dx.doi.org/10.1080/15397730903554633.

[15] Nurick GN, Gelman ME, Marshall NS. Tearing of blast loaded plates with clamped boundary conditions. Int J Impact Eng 1996;18(7–8):803–27. http://dx.doi.org/10.1016/s0734-743x(96)00026-7.

[16] LST. LS-DYNA | Livermore Software Technology Corp., URL https://www.lstc.com/products/ls-dyna.

[17] Curry R. Response of plates subjected to air-blast and buried explosions (Ph.D. thesis), University of Cape Town; 2017, p. 318.

[18] Curry RJ, Langdon GS. Transient response of steel plates subjected to close proximity explosive detonations in air. Int J Impact Eng 2017;102:102–16. http://dx.doi.org/10.1016/j.ijimpeng.2016.12.004.

[19] Chung Kim Yuen S, Nurick GN, Langdon GS, Iyer Y, Yuen SCK, Nurick GN, Langdon GS, Iyer Y. Deformation of thin plates subjected to impulsive load: Part III – an update 25 years on. Int J Impact Eng 2016;107:108–17. http://dx.doi.org/10.1016/j.ijimpeng.2016.06.010.

[20] Nurick GN, Martin JB. Deformation of thin plates subjected to impulsive loading - A review Part I: Theoretical considerations. Int J Impact Eng 1989;8(2):159–70.

[21] Jones N. Structural impact. 2nd ed.. New York: Cambridge University Press; 2012, p. 584. http://dx.doi.org/10.1155/1999/124792.

[22] Chakrabarty J. Applied plasticity. 2nd ed.. l: Springer Science+Business Media; 2010, p. 544. http://dx.doi.org/10.1007/b22134, arXiv:arXiv:1011.1669v3.

[23] Jones N. Recent studies on the dynamic plastic behavior of structures - An update. Appl Mech Rev 1996;49(10):S112—-S117. http://dx.doi.org/10.1115/1.3101962.

[24] Jones N. Recent studies on the dynamic plastic behavior of structures. Appl Mech Rev 1989;42(4):95–115.

[25] Jones N. Recent progress in the dynamic plastic behavior of structures. 1978, p. 44.

[26] Lomazzi L, Giglio M, Manes A. Analytical and empirical methods for the characterisation of the permanent transverse displacement of quadrangular metal plates subjected to blast load: Comparison of existing methods and development of a novel methodological approach. Int J Impact Eng 2021;154(March):103890. http://dx.doi.org/10.1016/j.ijimpeng.2021.103890.

[27] Hopkins HG, Prager W. On the dynamics of plastic circular plates. Z Angew Math Phys Zamp 1954;5(4):317–30. http://dx.doi.org/10.1007/BF01587827.

[28] Wang AJ, Hopkins HG. On the plastic deformation of built-in circular plates under impulsive load. J Mech Phys Solids 1954;3(1):22–37. http://dx.doi.org/10.1016/0022-5096(54)90036-8.

[29] Wang AJ. The permanent deflection of a plastic plate under blast loading. J Appl Mech 1955;22(3):375–6. http://dx.doi.org/10.1115/1.4011092.

[30] Micallef K, Fallah AS, Pope DJ, Louca LA. The dynamic performance of simply-supported rigid-plastic circular steel plates subjected to localised blast loading. Int J Mech Sci 2012;65(1):177–91. http://dx.doi.org/10.1016/j.ijmecsci.2012.10.001.

[31] Micallef K, Fallah AS, Pope DJ, Louca LA. Dynamic performance of simply supported rigid plastic circular thick steel plates subjected to localized blast loading. J Eng Mech 2014;140(1):159–71. http://dx.doi.org/10.1061/(asce)em.1943-7889.0000645.

[32] Cox AD, Morland LW. Dynamic plastic deformations of simply-supported square plates. J Mech Phys Solids 1959;7(4):229–41. http://dx.doi.org/10.1016/0022-5096(59)90022-5.

[33] Mehreganian N, Fallah AS, Louca LA. Plastic dynamic response of simply supported thick square plates subject to localised blast loading. Int J Impact Eng 2019;126:85–100. http://dx.doi.org/10.1016/j.ijimpeng.2018.12.010.

[34] Parkes EW. The permanent deformation of a cantilever struck transversely at its tip. Proc R Soc Lond A 1955;228(1175):462–76.

[35] Parkes EW. The permanent deformation of an encastre beam struck transversely at any point in its span. Proc Inst Civ Eng 1958;10(3):277–304.

[36] Wang XD, Yu TX. Parkes revisited: Effect of elastic deformation at the root of a cantilever beam. Int J Impact Eng 1991;11(2):197–209.

[37] Symonds PS, Fleming WT. Parkes revisited: On rigid-plastic and elastic-plastic dynamic structural analysis. Int J Impact Eng 1984;2(1):1–36. http://dx.doi.org/10.1016/0734-743X(84)90013-7.

[38] Hopkins HG. On the plastic theory of plates. Proc R Soc A 1957;241(1225):153–79, URL http://www.jstor.org/stable/2414705.

[39] Martin JB. Impulsive loading theorems for rigid-plastic continua. J Eng Mech Div 1964;90(5):27–42.

[40] Martin JB. Convergence to mode form solutions in impulsively loaded piecewise linear rigid-plastic structures. Tech. rep., 2, Great Britain: Pergamon Press Ltd.; 1983, p. 125–41.

[41] Martin JB, Symonds PS. Mode approximations for impulsively loaded rigid plastic structures. 1965, p. 61.

[42] Hudson GE. A theory of the dynamic plastic deformation of a thin diaphragm. J Appl Phys 1951;22(1):1–11.

[43] Jones N. Impulsive loading of a simply supported circular plate. Tech. rep., February, Division of Engineering Brown University Providence, Rhode Island; 1967.

[44] Mihailescu-Suliciu M, Wierzbicki T. Wave solution for an impulsively loaded rigid-plastic circular membrane. Arch Mech 2002;54(5–6):553–75.

[45] Wierzbicki T, Nurick GN. Large deformation of thin plates under localised impulsive loading. Int J Impact Eng 1996;18(7–8):899–918. http://dx.doi.org/10.1016/s0734-743x(96)00027-9.

[46] Cloete TJ, Nurick GN. On the influence of radial displacements and bending strains on the large deflections of impulsively loaded circular plates. Int J Mech Sci 2014;82:140–8. http://dx.doi.org/10.1016/j.ijmecsci.2014.02.026.

[47] Mehreganian N, S. Fallah A, Louca LA. Inelastic dynamic response of square membranes subjected to localised blast loading. Int J Mech Sci 2018;148:578–95. http://dx.doi.org/10.1016/j.ijmecsci.2018.09.017.

[48] Mehreganian N, Fallah AS, Louca LA. Nonlinear dynamics of locally pulse loaded square Föppl–von Kármán thin plates. Int J Mech Sci 2019;163(September). http://dx.doi.org/10.1016/j.ijmecsci.2019.105157.

[49] Jones N. Dynamic inelastic response of strain rate sensitive ductile plates due to large impact, dynamic pressure and explosive loadings. Int J Impact Eng 2014;74:3–15. http://dx.doi.org/10.1016/J.IJIMPENG.2013.05.003.

[50] Ploch J, Wierzbicki T. Bounds for large plastic deformations of dynamically loaded continua and structures. Int J Solids Struct 1981;17(2):183–95. http://dx.doi.org/10.1016/0020-7683(81)90074-3.

[51] Ronter ARS, Martin JB. Bounds for impulsively loaded plastic structures. J Eng Mech Div 1972;98(EM1):107–19.

[52] Rigby SE, Tyas A, Bennett T. Elastic-plastic response of plates subjected to cleared blast loads. Int J Impact Eng 2014;66:37–47. http://dx.doi.org/10.1016/J.IJIMPENG.2013.12.006.

[53] Biggs JM. Introduction to structural dynamics. New York, NY, USA: McGraw-Hill Book Company; 1964, p. 355.

[54] Nurick GN, Martin JB. Deformation of thin plates subjected impulsive loading–A review PART II: Experimental studies. Int J Impact Eng 1989;8(2):171–86.

[55] Rigby SE, Tyas A, Curry RJ, Langdon GS. Experimental measurement of specific impulse distribution and transient deformation of plates subjected to near-field explosive blasts. Exp Mech 2019;59(2):163–78. http://dx.doi.org/10.1007/s11340-018-00438-3.

[56] Pannell JJ, Panoutsos G, Cooke SB, Pope DJ, Rigby SE. Predicting specific impulse distributions for spherical explosives in the extreme near-field using a Gaussian function. Int J Prot Struct 2021;1–23. http://dx.doi.org/10.1177/2041419621993492.

[57] Nurick GN, Shave GC. The deformation and tearing of thin square plates subjected to impulsive loads - An experimental study. Int J Impact Eng 1996;18(1):99–116. http://dx.doi.org/10.1016/0734-743X(95)00018-2.

[58] Teeling-Smith RG, Nurick GN. The deformation and tearing of thin circular plates subjected to impulsive loads. Int J Impact Eng 1991;11(1):77–91. http://dx.doi.org/10.1016/0734-743X(91)90032-B.

[59] Clarke SD, Fay SD, Warren JA, Tyas A, Rigby SE, Elgy I. A large scale experimental approach to the measurement of spatially and temporally localised loading from the detonation of shallow-buried explosives. Meas Sci Technol 2015;26(1):1–10. http://dx.doi.org/10.1088/0957-0233/26/1/015001.

[60] McDonald B, Bornstein H, Langdon GS, Curry R, Daliri A, Orifici AC. Experimental response of high strength steels to localised blast loading. Int J Impact Eng 2018;115(January):106–19. http://dx.doi.org/10.1016/j.ijimpeng.2018.01.012.

[61] Mehreganian N, Louca LA, Langdon GS, Curry RJ, Abdul-Karim N. The response of mild steel and armour steel plates to localised air-blast loading-comparison of numerical modelling techniques. Int J Impact Eng 2018;115(May 2017):81–93. http://dx.doi.org/10.1016/j.ijimpeng.2018.01.010.

[62] Aune V, Fagerholt E, Hauge KO, Langseth M, Bø rvik T. Experimental study on the response of thin aluminium and steel plates subjected to airblast loading. Int J Impact Eng 2016;90:106–21. http://dx.doi.org/10.1016/j.ijimpeng.2015.11.017.

[63] Aune V, Valsamos G, Casadei F, Larcher M, Langseth M, Børvik T. Numerical study on the structural response of blast-loaded thin aluminium and steel plates. Int J Impact Eng 2017;99:131–44. http://dx.doi.org/10.1016/j.ijimpeng.2016.08.010.

[64] Elveli BS, Iddberg MB, Bø rvik T, Aune V. On the strength–ductility trade-off in thin blast-loaded steel plates with and without initial defects — An experimental study. Thin-Walled Struct 2022;171(November 2021):108787. http://dx.doi.org/10.1016/j.tws.2021.108787.

[65] Spranghers K, Vasilakos I, Lecompte D, Sol H, Vantomme J. Full-field deformation measurements of aluminium plates under free air blast loading. Exp Mech 2012;52(9):1371–84. http://dx.doi.org/10.1007/s11340-012-9593-5.

[66] Spranghers K, Vasilakos I, Lecompte D, Sol H, Vantomme J. Numerical simulation and experimental validation of the dynamic response of aluminum plates under free air explosions. Int J Impact Eng 2013;54:83–95. http://dx.doi.org/10.1016/j.ijimpeng.2012.10.014.

[67] Rigby S, Fuller B, Tyas A. Validation of near-field blast loading in LS-DYNA, 1, (August) (2018) 1–8.

[68] Granum H, Aune V, Bø rvik T, Hopperstad OS. Effect of heat-treatment on the structural response of blast-loaded aluminium plates with pre-cut slits. Int J Impact Eng 2019;132(February):103306. http://dx.doi.org/10.1016/j.ijimpeng.2019.05.020.

[69] Rayleigh J. The theory of sound. The theory of sound, Vol.. 1, Macmillan; 1894.

[70] Timoshenko S, Young DH. Vibration problems in engineering. Van Nostrand; 1955.

[71] Rao SS. Vibration of membranes. In: Vib. contin. syst.. John Wiley & Sons, Ltd; 2019, p. 427–63. http://dx.doi.org/10.1002/9781119424284.ch13, URL https://onlinelibrary.wiley.com/doi/abs/10.1002/9781119424284.ch13, (Chapter 13).

[72] Nicholson J. Bessel zero solver - file exchange - MATLAB central. 2022, URL https://uk.mathworks.com/matlabcentral/fileexchange/48403-bessel-zero-solver.

[73] Livermore Software Technology (LST). Keyword user's manual volume ii: material models R12, Vol. II. r12 ed.. Livermore, CA: Livermore Software Technology (LST), An ANSYS Company; 2020, p. 3099.

[74] Spranghers K, Lecompte D, Sol H, Vantomme J. Material characterization of blast loaded plates. Meca.Rma.Ac.Be 2012;(May):9–10, URL http://meca.rma.ac.be/nctam/ExperimentalTechniques/4{_}Spranghers.pdf.

[75] Weisstein EW. Parseval's Theorem - from Wolfram MathWorld, URL https://mathworld.wolfram.com/ParsevalsTheorem.html.